Article

High-Valent Nonheme Iron. Two Distinct Iron(IV) Species Derived from a Common Iron(II) Precursor

Michael P. Jensen, Miquel Costas, Raymond Y. N. Ho, Jzsef Kaizer, Antoni Mairata i Payeras, Eckard Mnck, Lawrence Que,, Jan-Uwe Rohde, and Audria Stubna

J. Am. Chem. Soc., **2005**, 127 (30), 10512-10525• DOI: 10.1021/ja0438765 • Publication Date (Web): 09 July 2005

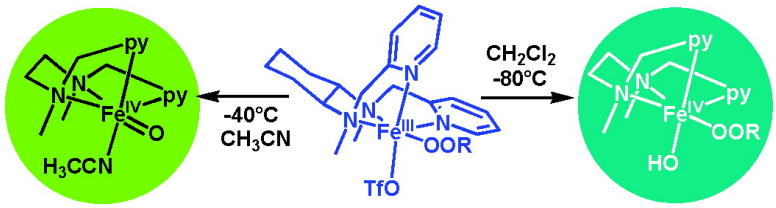

More About This Article

Additional resources and features associated with this article are available within the HTML version:

- Supporting Information
- Links to the 18 articles that cite this article, as of the time of this article download
- Access to high resolution figures
- Links to articles and content related to this article
- Copyright permission to reproduce figures and/or text from this article

View the Full Text HTML

Journal of the American Chemical Society is published by the American Chemical Society. 1155 Sixteenth Street N.W., Washington, DC 20036

J|A|C|S
ARTICLES
Published on Web 07/09/2005

High-Valent Nonheme Iron. Two Distinct Iron(IV) Species Derived from a Common Iron(II) Precursor

Michael P. Jensen,[†] Miquel Costas,[†] Raymond Y. N. Ho,[†] József Kaizer,[†] Antoni Mairata i Payeras,[†] Eckard Münck,*[,‡] Lawrence Que, Jr.,*[,†] Jan-Uwe Rohde,[†] and Audria Stubna[‡]

Contribution from the Department of Chemistry and the Center for Metals in Biocatalysis, University of Minnesota, Minneapolis, Minnesota 55455, and the Department of Chemistry, Carnegie Mellon University, Pittsburgh, Pennsylvania 15213

Received October 7, 2004; E-mail: emunck@cmu.edu; que@chem.umn.edu

Abstract: The reaction of [Fe^{II}(β-BPMCN)($OTf)_2$] (**1**, BPMCN = *N*,*N*′-bis(2-pyridylmethyl)-*N*,*N*′-dimethyl-*trans*-1,2-diaminocyclohexane) with ^{t}BuOOH at low-temperature yields alkylperoxoiron(III) intermediates **2** in CH_2Cl_2 and **2-NCMe** in CH_3CN. At −45 °C and above, **2-NCMe** converts to a pale green species **3** (λ_{max} = 753 nm, ϵ = 280 M^{-1} cm^{-1}) in 90% yield, identified as [Fe^{IV}(O)(BPMCN)($NCCH_3$)]$^{2+}$ by comparison to other nonheme [Fe^{IV}(O)(L)]$^{2+}$ complexes. Below −55 °C in CH_2Cl_2, **2** decays instead to form deep turquoise **4** (λ_{max} = 656, 845 nm; ϵ = 4000, 3600 M^{-1} cm^{-1}), formulated to be an unprecedented alkylperoxoiron(IV) complex [Fe^{IV}(BPMCN)(OH)(OO^{t}Bu)]$^{2+}$ on the basis of Mössbauer, EXAFS, resonance Raman, NMR, and mass spectral evidence. The reactivity of **1** with ^{t}BuOOH in the two solvents reveals an unexpectedly rich iron(IV) chemistry that can be supported by the BPMCN ligand.

1. Introduction

Oxoiron(IV) species are typically invoked as the reactive intermediates in both heme and nonheme iron-dependent oxygenases. While the existence of high-valent oxoiron species has been well established for some time in the chemistry of heme enzymes,[1,2] as well as iron porphyrin model compounds,[3] only more recently have corresponding nonheme iron examples been identified. Nonheme iron oxygenases can thus far be divided between two classes, those with carboxylate-bridged diiron(II) active sites[4,5] and those with monoiron(II) active sites having the 2-His-1-carboxylate facial triad motif.[6] High-valent intermediates in the dinuclear class include intermediate **Q** of methane monooxygenase (MMO-**Q**),[7] postulated to have an $Fe^{IV}_2(\mu$-O)$_2$ diamond core structure,[8] and the only biological intermediate known to be capable of methane hydroxylation,[9] and intermediate **X** of the diiron ribonucleotide reductase,[10] best described as an Fe^{III}−O−Fe^{IV} species and the oxidant responsible for generating the catalytically essential tyrosyl radical.[11] Very recently, a mononuclear oxoiron(IV) intermediate has been trapped in the reaction of the 2-oxoglutarate-dependent enzyme TauD with O_2 in the presence of substrate and cofactor.[12−15] These examples serve as biological precedents for the iron(IV) oxidation state in nonporphyrin ligand environments.

We have recently been successful in obtaining well characterized synthetic analogues of high-valent nonheme iron species, reporting the crystal structures of [$Fe_2(\mu$-O)$_2$(5-Et$_3$TPA)$_2$]$^{3+}$ (TPA, tris(2-pyridylmethyl)amine), a diiron(III,IV) complex with an $Fe_2(\mu$-O)$_2$ core,[16] and [Fe^{IV}(O)(TMC)($NCCH_3$)]$^{2+}$ (TMC, 1,4,8,11-tetramethyl-1,4,8,11-tetraazacyclotetradecane), an oxoiron(IV) complex.[17] Complexes related to the latter have also been spectroscopically characterized with the tetradentate tripodal TPA ligand[18] and the pentadentate ligands N4Py, Bn-TPEN, Me-TPEN, and Me-TPPN (N4Py = bis(2-pyridylmethyl)bis(2-pyridyl)methylamine; Bn-TPEN = *N*-benzyl-

[†] University of Minnesota.
[‡] Carnegie Mellon University.

(1) Sono, M.; Roach, M. P.; Coulter, E. D.; Dawson, J. H. *Chem. Rev.* **1996**, *96*, 2841−2887.
(2) Schlichting, I.; Berendzen, J.; Chu, K.; Stock, A. M.; Maves, S. A.; Benson, D. E.; Sweet, R. M.; Ringe, D.; Petsko, G. A.; Sligar, S. G. *Science* **2000**, *287*, 1615−1622.
(3) Groves, J. T.; Han, Y.-Z. *Models and Mechanisms of Cytochrome P450 Action*, 2nd ed.; Ortiz de Montellano, P. R., Ed.; Plenum Press: New York, 1995; pp 3−48.
(4) Wallar, B. J.; Lipscomb, J. D. *Chem. Rev.* **1996**, *96*, 2625−2658.
(5) Tshuva, E. Y.; Lippard, S. J. *Chem. Rev.* **2004**, *104*, 987−1012.
(6) Costas, M.; Mehn, M. P.; Jensen, M. P.; Que, L., Jr. *Chem. Rev.* **2004**, *104*, 939−986.
(7) Merkx, M.; Kopp, D. A.; Sazinsky, M. H.; Blazyk, J. L.; Müller, J.; Lippard, S. J. *Angew. Chem., Int. Ed.* **2001**, *40*, 2782−2807.
(8) Shu, L.; Nesheim, J. C.; Kauffmann, K.; Münck, E.; Lipscomb, J. D.; Que, L., Jr. *Science* **1997**, *275*, 515−518.
(9) Lipscomb, J. D.; Que, L., Jr. *J. Biol. Inorg. Chem.* **1998**, *3*, 331−336.
(10) Bollinger, J. M., Jr.; Edmondson, D. E.; Huynh, B. H.; Filley, J.; Norton, J.; Stubbe, J. *Science* **1991**, *253*, 292−298.
(11) Sturgeon, B. E.; Burdi, D.; Chen, S.; Huynh, B.-H.; Edmondson, D. E.; Stubbe, J.; Hoffman, B. M. *J. Am. Chem. Soc.* **1996**, *118*, 7551−7557.
(12) Price, J. C.; Barr, E. W.; Tirupati, B.; Bollinger, J. M., Jr.; Krebs, C. *Biochemistry* **2003**, *42*, 7497−7508.
(13) Price, J. C.; Barr, E. W.; Glass, T. E.; Krebs, C.; Bollinger, J. M., Jr. *J. Am. Chem. Soc.* **2003**, *125*, 13008−13009.
(14) Riggs-Gelasco, P. J.; Price, J. C.; Guyer, R. B.; Brehm, J. H.; Barr, E. W.; Bollinger, J. M., Jr.; Krebs, C. *J. Am. Chem. Soc.* **2004**, *126*, 8108−8109.
(15) Proshlyakov, D. A.; Henshaw, T. F.; Monterosso, G. R.; Ryle, M. J.; Hausinger, R. P. *J. Am. Chem. Soc.* **2004**, *126*, 1022−1023.
(16) Hsu, H.-F.; Dong, Y.; Shu, L.; Young, V. G., Jr.; Que, L., Jr. *J. Am. Chem. Soc.* **1999**, *121*, 5230−5237.
(17) Rohde, J.-U.; In, J. H.; Lim, M. H.; Brennessel, W. W.; Bukowski, M. R.; Stubna, A.; Münck, E.; Nam, W.; Que, L., Jr. *Science* **2003**, *299*, 1037−1039.
(18) Lim, M. H.; Rohde, J.-U.; Stubna, A.; Bukowski, M. R.; Costas, M.; Ho, R. Y. N.; Münck, E.; Nam, W.; Que, L., Jr. *Proc. Natl. Acad. Sci. U.S.A.* **2003**, *100*, 3665−3670.

10.1021/ja0438765 CCC: $30.25

Scheme 1. [Fe(β-BPMCN)(OTf)$_2$] + ^{t}BuOOH Reaction Landscape

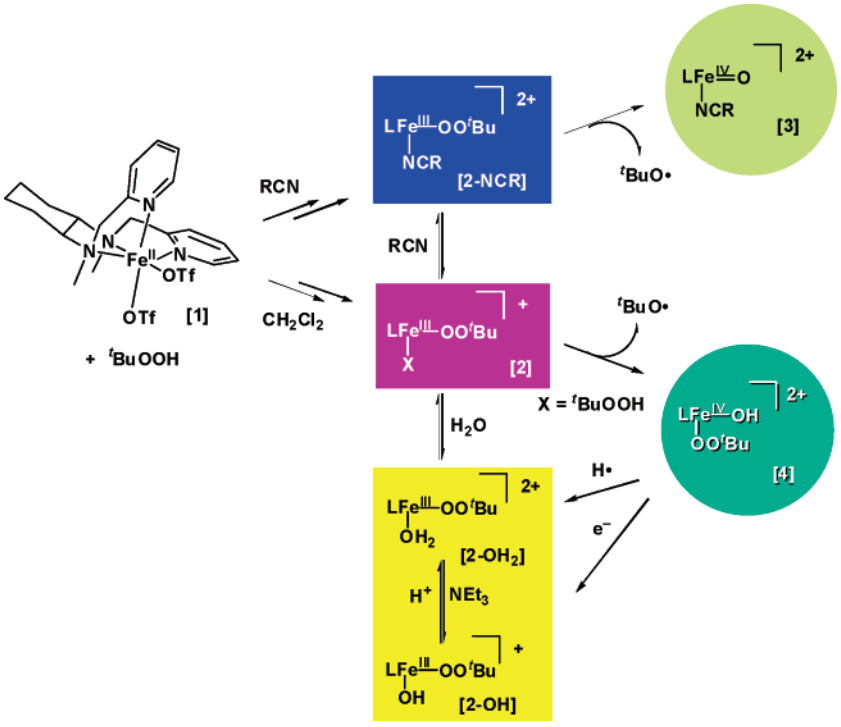

N,*N*′,*N*′-tris(2-pyridylmethyl)-1,2-diaminoethane; Me-TPEN = *N*-methyl-*N*,*N*′,*N*′-tris(2-pyridylmethyl)-1,2-diaminoethane; Me-TPPN = *N*-methyl-*N*,*N*′,*N*′-tris(2-pyridylmethyl)-1,3-diaminopropane).[19,20] In addition, Collins and co-workers have recently reported the crystal structure of a (μ-oxo)diiron(IV) complex.[21] These synthetic complexes serve as a starting point for exploring the yet largely uncharted nonheme oxoiron(IV) reaction landscape.

Prior to our discovery of the oxoiron(IV) class of complexes, we described a distinct iron(IV) species obtained by oxidation of [Fe^{II}(β-BPMCN)(OTf)$_2$] (**1**) with ^{t}BuOOH in CH_2Cl_2 solution at −80 °C.[22] This oxidation product, designated herein as **4**, was demonstrated to be a low-spin iron(IV) complex by Mössbauer spectroscopy and exhibited intense low-energy absorption features (λ_{max} = 656, 845 nm; ϵ = 4000, 3600 M^{-1} cm^{-1}) that impart a deep turquoise color, quite unlike the pale green of the oxoiron(IV) complexes, which exhibit only weak visible and near-IR ligand field bands.[17−19,23] Analysis of EXAFS and resonance Raman data led to formulation of this unique iron(IV) product as [Fe$^{IV}_2$(μ-O)$_2$(β-BPMCN)$_2$](OTf)$_4$,[22] modeling the diiron(IV,IV) oxidation state and diamond core structure of MMO-**Q**.

Given this background, it would appear that **4** is a dimeric form of the yet unknown BPMCN analogue of the oxoiron(IV) complexes just described. For example, mononuclear [Fe^{IV}(O)(TPA)(NCMe)]$^{2+}$ can be obtained by reaction of its iron(II) precursor with ^{t}BuOOH in CH_3CN;[24] **4** is formed by a similar reaction, but in noncoordinating CH_2Cl_2. Attempting to connect these two reaction manifolds, we have further investigated the reaction of **1** with ^{t}BuOOH in both CH_3CN and CH_2Cl_2. Evidence is presented for the expected formation of a mononuclear oxoiron(IV) complex in CH_3CN, designated as **3**. The generation of **4** in CH_2Cl_2 is confirmed, but additional spectroscopic data to be detailed herein lead us to discard the originally proposed diamond core structure for **4**[22] and to reformulate it instead as an unprecedented alkylperoxoiron(IV) complex, [Fe^{IV}(BPMCN)(OH)(OO^{t}Bu)]$^{2+}$. This investigation thus reveals an unexpectedly complex reaction landscape summarized in Scheme 1, leading to novel iron(IV) species.

2. Experimental Section

Materials and Synthesis. All reagents were purchased from commercial sources and used as received, unless noted otherwise. CH_3CN and diethyl ether were purified by passage through alumina, and CH_2Cl_2 was distilled from CaH_2. Solvents were degassed by several argon-vacuum cycles and stored in an anaerobic glovebox. Ferrocene was sublimed before use. A literature synthesis was used to prepare $(CD_3)_3COOH$.[25] $^{57}Fe(OTf)_2(NCCH_3)_2$ was prepared by digestion of isotopic iron metal with hydrochloric acid and treatment of the residue with Me_3SiOTf in CH_3CN. The preparation of **1** was carried out as previously described.[26,27]

Physical Methods. Electronic absorption spectra were recorded on a Hewlett-Packard (Agilent) 8453 diode array spectrophotometer (190−1100-nm range) in quartz cuvettes cooled to the desired temperature, either in a methanol-filled dewar fitted with quartz windows

(19) Kaizer, J.; Klinker, E. J.; Oh, N. Y.; Rohde, J.-U.; Song, W. J.; Stubna, A.; Kim, J.; Nam, W.; Münck, E.; Que, L., Jr. *J. Am. Chem. Soc.* **2004**, *126*, 472−473.
(20) Balland, V.; Charlot, M.-F.; Banse, F.; Girerd, J.-J.; Mattioli, T. A.; Bill, E.; Bartoli, J.-F.; Battioni, P.; Mansuy, D. *Eur. J. Inorg. Chem.* **2004**, 301−308.
(21) Ghosh, A.; de Oliveira, F. T.; Yano, T.; Nishioka, T.; Beach, E. S.; Kinoshita, I.; Münck, E.; Ryabov, A. D.; Horwitz, C. P.; Collins, T. J. *J. Am. Chem. Soc.* **2005**, *127*, 2505−2513.
(22) Costas, M.; Rohde, J.-U.; Stubna, A.; Ho, R. Y. N.; Quaroni, L.; Münck, E.; Que, L., Jr. *J. Am. Chem. Soc.* **2001**, *123*, 12931−12932.
(23) Decker, A.; Rohde, J.-U.; Que, L., Jr.; Solomon, E. I. *J. Am. Chem. Soc.* **2004**, *126*, 5378−5379.
(24) Kaizer, J.; Costas, M.; Que, L., Jr. *Angew. Chem., Int. Ed.* **2003**, *42*, 3671−3673.
(25) Sobolev, A. P.; Babushkin, D. E.; Talsi, E. P. *J. Mol. Catal.* **2000**, *159*, 233−245.
(26) Costas, M.; Tipton, A. K.; Chen, K.; Jo, D.-H.; Que, L., Jr. *J. Am. Chem. Soc.* **2001**, *123*, 6722−6723.
(27) Costas, M.; Que, L., Jr. *Angew. Chem., Int. Ed.* **2002**, *41*, 2179−2181.

and cooled by a circulating bath equipped with a thermostat (Neslab) or in a liquid nitrogen cryostat (Unisoku). ^{1}H NMR spectra (499.9 MHz) were obtained on a Varian Inova VI-500 spectrometer and referenced to residual solvent. ^{2}H NMR spectra (46.1 MHz) were obtained on a Varian Inova VI-300 spectrometer and referenced to internal solvent; temperature calibration was performed by the methanol method, and curve fits were calculated using Grams 32 Spectral Notebook (Thermo Galactic). Low-resolution electrospray mass spectra were recorded on a Bruker Biotof II spectrometer.

Resonance Raman spectra were collected on an Acton AM-506 spectrometer (2400-groove grating) using Kaiser Optical holographic super-notch filters with a Princeton Instruments liquid N_2-cooled (LN-1100PB) CCD detector with 4 or 2 cm^{-1} spectral resolution. Spectra were obtained using a backscattering geometry on liquid N_2 frozen samples with laser excitation from either a Spectra Physics 2030 argon ion laser and a 375B CW dye (Rhodamine 6G) or a Spectra Physics Beamlock 2060 krypton laser. Raman frequencies were referenced to indene.

Mössbauer spectra were recorded with two spectrometers, using Janis Research Super-Varitemp dewars that allowed studies in applied magnetic fields up to 8.0 T in the temperature range from 1.5 to 200 K. Mössbauer spectral simulations were performed using the WMOSS software package (WEB Research, Edina, MN). Isomer shifts are quoted relative to Fe metal at 298 K. EPR spectra were recorded on a Bruker EPP 300 spectrometer equipped with an Oxford ESR 910 liquid helium cryostat and an Oxford temperature controller. Software for EPR analysis was provided by Dr. Michael P. Hendrich of Carnegie Mellon University.

Fe K-edge X-ray absorption spectra were recorded on frozen solutions at 5−15 K over the energy range 6.9−8.0 keV at beamline X9B of the National Synchrotron Light Source (NSLS, Brookhaven National Laboratory) and at beamline 7−3 of the Stanford Synchrotron Radiation Laboratory (SSRL), as described previously.[28,29] Storage ring conditions: 3 GeV, 50−100 mA (SSRL), and 2.8 GeV, 100−300 mA (NSLS). The beam vertical aperture of the pre-monochromator slits was 1 mm. Contamination of higher harmonics radiation was minimized by detuning the Si(220) double-crystal monochromator by 50% at ~8 keV (beamline 7−3 at SSRL) and by a harmonic rejection mirror (beamline X9B at NSLS), respectively. The horizontal spot size on the sample was 4−5 mm in most cases. Spectra were measured with 10-eV steps below the edge, 0.3-eV steps in the edge region, and steps equivalent to 0.05 $Å^{-1}$ increments above the edge (region borders were 6880, 7090, and 7140 eV at beamline 7-3, SSRL, and 6932, 7102, and 7137 eV at beamline X9B, NSLS). The monochromator was calibrated using the K-edge energy of iron foil at 7112.0 eV. The data were obtained as fluorescence excitation spectra ($A_{exp}(C_f/C_0)$) using a solid-state germanium detector (Canberra). The treatment of raw EXAFS data to yield $\chi(k)$ is discussed in detail elsewhere.[30,31] Our specific data analysis protocol using the programs EXAFSPAK[32] and SSExafs[28,33] was previously described.[34] The edge was modeled as an integral of a 75% Gaussian and 25% Lorentzian peak. The heights, positions, and widths (at half-height) of pre-edge peaks were refined using a Gaussian function. Refinements with multiple peaks were constrained to have a common width for all peaks. Pre-edge peak areas are given as the percentage of Fe K-edge height (eV). An artifact in the data of **2-NCPr** at ca. 7620−7645 eV ($k \approx 11.4-11.7$ $Å^{-1}$), also found in the incident beam (I_0), was removed from the raw EXAFS data.

Preparation of Mössbauer/XAS Samples. Treatment of 33% ^{57}Fe-enriched **1** with 5 equiv of ^{t}BuOOH (~0.15 mmol, 5−6 M ^{t}BuOOH in nonane) in 5 mL of PrCN at −70 °C resulted in slow formation of $[Fe^{III}(\beta\text{-BPMCN})(OO^tBu)(NCPr)]^{2+}$ (**2-NCPr**). A reaction in CH_3CN at −25 °C resulted in rapid initial formation of **2-NCMe**, which converted on standing 5 min to $[Fe^{IV}(O)(\beta\text{-BPMCN})(NCMe)]^{2+}$ (**3**). The product solutions of **2-NCPr** and **3** were transferred into a Mössbauer/XAS sample cell precooled with liquid nitrogen and allowed to freeze. Mössbauer spectra were recorded before and after the XAS experiment, and the concentrations of all iron species present were determined. Treatment of ^{57}Fe-enriched **1** in CH_2Cl_2 solution at −80 °C with 10 equiv of ^{t}BuOOH (5.4 M in nonane) resulted in the immediate formation of $[Fe^{III}(\beta\text{-BPMCN})(OO^tBu)]^{2+}$ (**2**), which converted to **4** on standing overnight in a −90 °C freezer. Because CH_2Cl_2 has a large extinction coefficient for 14.4-KeV γ-rays, demanding frozen solution samples with less than a 0.08-cm path length compared to 0.5 cm for a typical experiment, obtaining Mössbauer or XAS spectra in CH_2Cl_2 solution is technically unfeasible at the present time. Layering of cold pentane onto the CH_2Cl_2 solution eventually precipitated **4** as a blue polycrystalline solid. The solid was washed with cold pentane and redissolved in cold butyronitrile. The Mössbauer/XAS sample was prepared in the fashion described above; again, Mössbauer experiments were carried out both before and after the XAS experiment.

3. Results

We describe in this paper the reaction chemistry of $[Fe^{II}(\beta\text{-BPMCN})(OTf)_2]$ (**1**) at millimolar concentrations with excess ^{t}BuOOH in cold CH_2Cl_2 or organonitrile solution, as summarized in Scheme 1. Depending on the folding of the racemic BPMCN ligand, topologically distinct and rigid iron complexes can be obtained, as previously described.[27] Of interest here is the *cis*-beta configuration (Scheme 1) that supports a high-spin ($S = 2$) $Fe^{II}(OTf)_2$ complex **1** and yields inequivalent cis triflate binding sites disposed trans to one amine and one pyridine donor.[22,26,27] A *cis*-alpha iron(II) complex with trans pyridines is also known,[27] but this isomer does not form the intermediates described herein; the planar trans isomer has yet to be observed. As indicated by the appearance of a characteristic iron(II)-pyridine MLCT band at 375 nm, organonitriles solvate **1**, displacing the weakly bound triflates to give a complex dication that significantly crosses to a diamagnetic low-spin state at −45 °C.[35]

3.1. Reaction of 1 with ^{t}BuOOH: Formation of Alkylperoxoiron(III) Complexes 2. Addition of ^{t}BuOOH in a 5−10-fold excess to a solution of **1** in CH_2Cl_2 at −70 °C resulted in the immediate formation of an intense purple chromophore ($\lambda_{max} = 566$ nm, $\epsilon = 2500$ M^{-1} cm^{-1}) arising from the alkylperoxoiron(III) complex **2** (Figure 1B). This assignment is consistent with previous spectroscopy of alkylperoxoiron(III) complexes supported by the tetradentate tripodal TPA ligand, which exhibit similar absorption assigned to Fe^{III}-OOR LMCT.[36−38] Addition of acetonitrile (0.6 M) to the CH_2Cl_2 solution prompted a color change from purple to blue, corresponding to a red shift of the CT chromophore to 600 nm ($\epsilon = 2500$ M^{-1} cm^{-1}). The same

(28) Scarrow, R. C.; Maroney, M. J.; Palmer, S. M.; Roe, A. L.; Que, L., Jr.; Salowe, S. P.; Stubbe, J. *J. Am. Chem. Soc.* **1987**, *109*, 7857−7864.
(29) Shu, L.; Chiou, Y.-M.; Orville, A. M.; Miller, M. A.; Lipscomb, J. D.; Que, L., Jr. *Biochemistry* **1995**, *34*, 6649−6659.
(30) Scott, R. A. *Methods Enzymol.* **1985**, *11*, 414−459.
(31) Teo, B.-K. *EXAFS Spectroscopy, Techniques and Applications*; Plenum: New York, 1981.
(32) George, G. N.; Pickering, I. *EXAFSPAK*; Stanford Synchrotron Radiation Laboratory, Stanford Linear Accelerator Center, 2000.
(33) Scarrow, R. C.; Trimitsis, M. G.; Buck, C. P.; Grove, G. N.; Cowling, R. A.; Nelson, M. J. *Biochemistry* **1994**, *33*, 15023−15035.
(34) Rohde, J.-U.; Torelli, S.; Shan, X.; Lim, M. H.; Klinker, E. J.; Kaizer, J.; Chen, K.; Nam, W.; Que, L., Jr. *J. Am. Chem. Soc.* **2004**, *126*, 16750−16761.
(35) Jensen, M. P.; Lange, S. J.; Mehn, M. P.; Que, E. L.; Que, L., Jr. *J. Am. Chem. Soc.* **2003**, *125*, 2113−2128.
(36) Zang, Y.; Kim, J.; Dong, Y.; Wilkinson, E. C.; Appelman, E. H.; Que, L., Jr. *J. Am. Chem. Soc.* **1997**, *119*, 4197−4205.
(37) Lehnert, N.; Ho, R. Y. N.; Que, L., Jr.; Solomon, E. I. *J. Am. Chem. Soc.* **2001**, *123*, 8271−8290.
(38) Lehnert, N.; Ho, R. Y. N.; Que, L., Jr.; Solomon, E. I. *J. Am. Chem. Soc.* **2001**, *123*, 12802−12816.

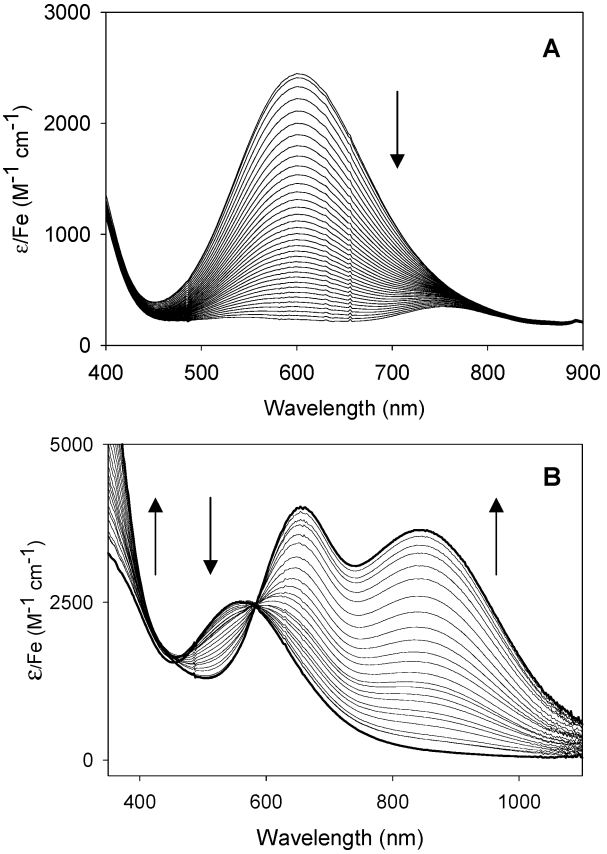

Figure 1. Visible−NIR spectral changes accompanying decay of **2-NCMe** in CH_3CN with 0.3 M added H_2O over 1 h at −45 °C (A) and of **2** in CH_2Cl_2 over 2 h at −67 °C (B).

600-nm chromophore was also obtained by oxidation of **1** in wet (0.3 M H_2O) CH_3CN at −45 °C (Figure 1A), the added water being necessary to accelerate the conversion of **1** to **2** relative to decay of the latter. Since the alkylperoxo complex intermediates **2-NCMe** in CH_3CN and **2** in CH_2Cl_2 were unstable and decayed to form distinct high-valent complexes (Figure 1), solutions of these species were frozen at the appropriate time to allow for further spectroscopic characterization.

3.1.1. Characterization of 2-NCR in Organonitrile Solutions. The EPR spectrum of **2** in frozen CH_3CN showed signals at $g = 2.20$, 2.14, and 1.97, indicative of an $S = {}^1/_2$ species. We thus designate this species as **2-NCMe**, with a solvent molecule occupying the sixth coordination site to generate the low-spin iron(III) center. When studied in a frozen PrCN glass, the corresponding **2-NCPr** intermediate exhibited sharper signals (Figure 2A) that resolved into two $S = {}^1/_2$ species with $g = 2.165$, 2.124, 1.964 (47%) and $g = 2.185$, 2.124, 1.970 (42%). The sample also contained a minor $S = {}^5/_2$ iron(III) species with $E/D \approx 1/3$ that represents about 11% of the total spin concentration. The observed g_{max} values support coordination of the organonitrile as the sixth ligand according to the correlations of Talsi for $[Fe^{III}(TPA)(OOR)(X)]$ species.[39] The appearance of two similar low-spin species might be attributed to formation of positional isomers, where the alkylperoxo moiety is disposed trans to either amine or pyridine (Scheme 1). However, other less obvious rationales are possible, since two low-spin species with slightly different *g*-values were reported

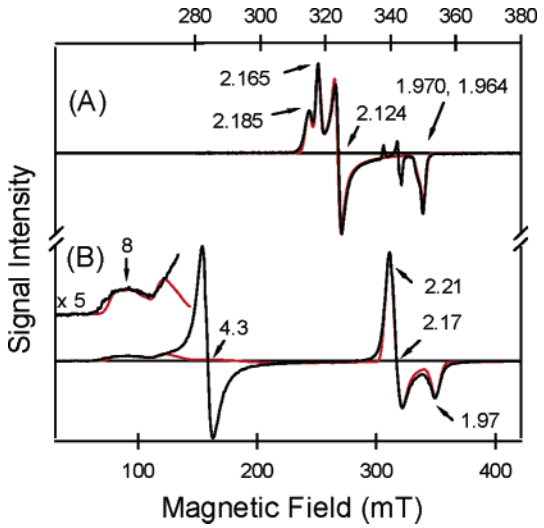

Figure 2. EPR spectra of **2** in PrCN (A) and in CH_2Cl_2 (B) recorded at 15 K using 20-mW applied power and a modulation amplitude of 0.98 mT at 100 kHz. The solid red lines are the spectral simulations described in the text.

for the hydroperoxo complex $[Fe^{III}(N4Py)(\eta^1\text{-OOH})]^{2+}$, where the pentadentate supporting ligand cannot accommodate such isomerism.[40]

In agreement with the EPR data, the resonance Raman spectrum of **2-NCMe** exhibits features at 490, 685, and 793 cm^{-1} (Table 1 and Figure 3A) that match well with those observed for low-spin $[Fe^{III}(TPA)(OO^tBu)(NCCH_3)]^{2+}$.[36] These vibrations correspond, respectively, to a *tert*-butyl deformation, a predominantly Fe−O stretching mode, and an O−O stretch.[37] The frequencies reflect the relatively strong Fe−O and weak O−O bonding associated with a low-spin alkylperoxoiron(III) center.[37,38] Spectra of **2-NCMe** prepared using $(CD_3)_3COOH$ and $^tBu^{18}O^{18}OH$ exhibited isotope effects on the modes that conform to the given assignments (Table 1 and Figure S1 in the Supporting Information). Comparable isotope shifts and increased spectral complexity were reported for the TPA analogue,[36] which has been studied in detail.[37]

Structural information for **2-NCR** was obtained from analysis of its X-ray absorption spectrum (Figure 4A). Complex **2-NCPr** exhibited an Fe K-edge at 7124.1 eV, consistent with an iron(III) oxidation state.[34] Pre-edge peaks at 7113.5 and 7115.7 eV that can be assigned to 1s→3d transitions were also observed (Figure S2 in the Supporting Information); the sum of the respective peak areas of 6.4(2) and 1.2(2) units falls into the range typically found for six-coordinate iron complexes (4−10 units).[41,42] Similar splitting patterns have been observed for other low-spin iron(III)-peroxo complexes.[34,43]

The Fourier transform (r' space) of the EXAFS region of **2-NCPr** exhibits prominent features centered at $r' = 1.6$, 1.9, and 2.2 Å with a shoulder at 1.2 Å (Figures 4B, 5A), where r' corresponds to the actual metal-scatterer distance r after a phase shift correction of approximately 0.4 Å ($r \approx r' + 0.4$ Å). The

(39) Lobanova, M. V.; Bryllakov, K. P.; Duhan, E. A.; Talsi, E. P. *Mendeleev Commun.* **2003**, 175−177.
(40) Roelfes, G.; Vrajmisu, V.; Chen, K.; Ho, R. Y. N.; Rohde, J.-U.; Zondervan, C.; la Crois, R. M.; Schudde, E. P.; Lutz, M.; Spek, A. L.; Hage, R.; Feringa, B. L.; Münck, E.; Que, L., Jr. *Inorg. Chem.* **2003**, *42*, 2639−2653.
(41) Roe, A. L.; Schneider, D. J.; Mayer, R.; Pyrz, J. W.; Widom, J.; Que, L., Jr. *J. Am. Chem. Soc.* **1984**, *106*, 1676−1681.
(42) Westre, T. E.; Kennepohl, P.; DeWitt, J. G.; Hedman, B.; Hodgson, K. O.; Solomon, E. I. *J. Am. Chem. Soc.* **1997**, *119*, 6297−6314.
(43) Koehntop, K. D.; Rohde, J.-U.; Costas, M.; Que, L., Jr. *J. Chem. Soc., Dalton Trans.* **2004**, 3191−3198.

Table 1. Raman Vibrations (cm^{-1}) of the Fe−OOR Unit

compound	oxidant	δ(^{t}Bu)	ν(Fe–O)	ν(O–^{t}Bu)	ν(O–O)
2-NCMe	^{t}Bu^{16}O^{16}OH	490	685		793
	^{t}Bu^{18}O^{18}OH	483	641, 653, 660, 664, 681	745	762
	$(CD_3)_3COOH$	434, 460	665, 694	730	782, 807
2 (ls) in CH_2Cl_2	^{t}Bu^{16}O^{16}OH		680[a]		789
	^{t}Bu^{18}O^{18}OH	476	653, 661		*a*
	$(CD_3)_3COOH$	426	665		802
2 (hs) in CH_2Cl_2	^{t}Bu^{16}O^{16}OH	474	628, 637, 647, 653		832, 851, 882
	^{t}Bu^{18}O^{18}OH	468	605, 617		801, 821, 851
	$(CD_3)_3COOH$	409	620		855, 877
$[Fe^{III}(TPA)(OO^tBu)(NCMe)]^{2+}$ [b]		490	696		796
$[Fe^{III}(6\text{-}Me_3\text{-}TPA)(OO^tBu)]^{2+}$ [b]		468	647		843, 881
4 in CH_2Cl_2	^{t}Bu^{16}O^{16}OH	477	680, 688	764	832, 845
		487	641(sh), 653, 660(sh)		778
	^{t}Bu^{18}O^{18}OH	474	657, 665	748[c]	789, 799
		483	628, 644		733[a,c]
4 in MeOH	^{t}Bu^{16}O^{16}OH	476	678, 685	764	832, 846
		487	640(sh), 652, 658(sh)		776
	$(CD_3)_3COOH$	432	659, 691	731	834, 845
			635, 643(sh)		771, 785
	^{t}Bu^{16}O^{18}OH	475	657, 663	765	817
		484	627, 643		755
2-OH (**4** + Et_3N)	^{t}Bu^{16}O^{16}OH	461	629		844, 891

[a] Obscured by solvent modes. [b] In CH_3CN, ref 36. [c] In CD_2Cl_2.

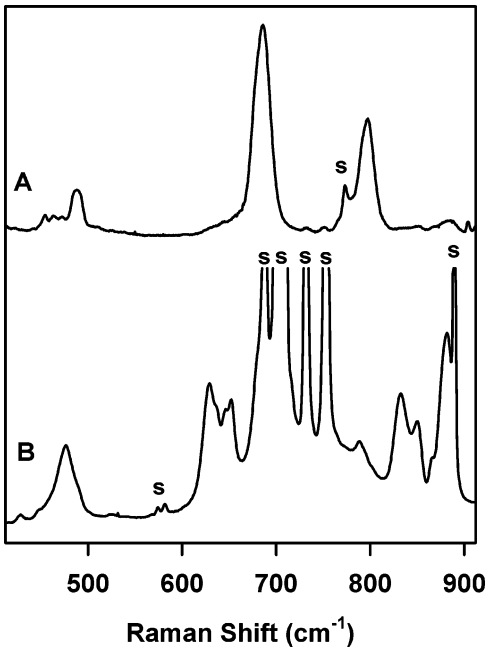

Figure 3. Resonance Raman spectra of **2-NCMe** in CH_3CN (A) and **2** in CH_2Cl_2 (B) recorded using 647.1-nm excitation. The peaks labeled "s" are solvent modes.

first coordination sphere of the low-spin iron(III) center was fit well by two shells of N/O atoms (fit 4, Table 2 and Table S1 in the Supporting Information): a one-atom subshell at $r = 1.81$ Å corresponding to the oxygen scatterer of the Fe−OO^{t}Bu moiety and another subshell at 1.99 Å representing the nitrogen donor atoms of the tetradentate BPMCN ligand, as well as the ligated solvent molecule. The latter distance is comparable to typical Fe−N bond lengths determined by X-ray crystallography of low-spin iron(III) complexes.[36] Furthermore, inclusion of an outer-sphere shell of six carbon atoms at 2.85 Å significantly improved the fit (Table 2, compare fits **2**-3 and **2**-4). This shell arises from the carbon atoms adjacent to the nitrogen donor atoms on the BPMCN ligand; for example, an X-ray crystal structure determination for low-spin $[Fe^{II}(\beta\text{-BPMCN})(NCCH_3)_2]^{2+}$

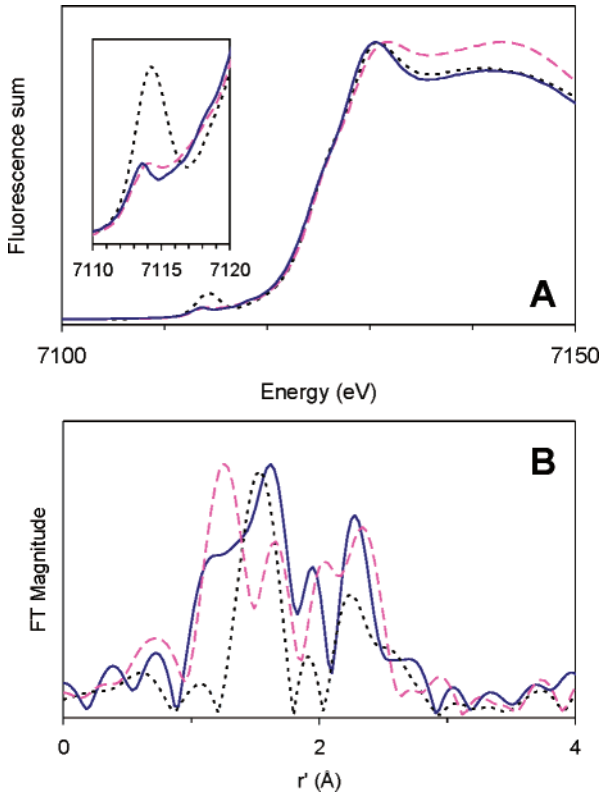

Figure 4. Comparison of the XAS data for of **2-NCPr** (—), **3** (···), and **4** (- - -). (A) Fe K-edge X-ray absorption near-edge structures (XANES, fluorescence excitation) with respective edge energies at 7124.1, 7124.6, and 7125.5 eV; (B) Fourier transforms (r' space) of the Fe K-edge EXAFS data ($k^3\chi(k)$), normalized to the height of the strongest peak. See Table 3 for further details.

revealed six such carbon atoms in the range 2.82−2.91 Å (average = 2.85 ± 0.03 Å) from the metal.[44] Thus, the accumulated spectroscopic data are consistent with the formulation of **2** in organonitrile solvents as $[Fe^{III}(BPMCN)(OO^tBu)(NCR)]^{2+}$ or **2-NCR**.

(44) Costas, M.; Young, V. G., Jr.; Que, L., Jr., unpublished results.

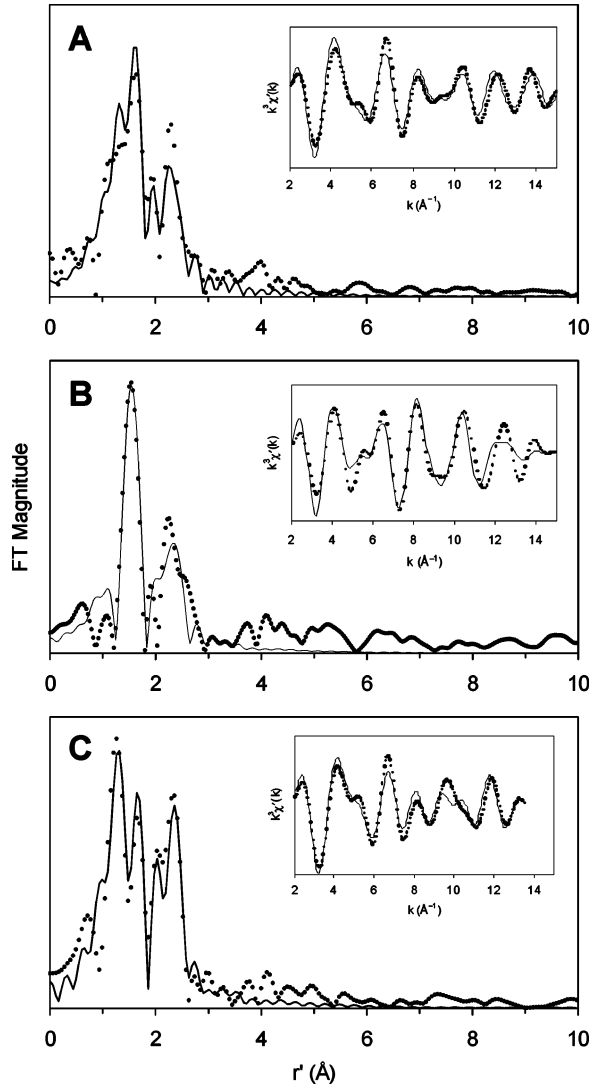

Figure 5. Fourier transforms of the Fe K-edge EXAFS data ($k^3\chi(k)$) and Fourier-filtered EXAFS spectra ($k^3\chi'(k)$, inset) of the following: **2-NCPr**, Fourier transformed range $k = 2-15$ Å^{-1}; experimental data (•••) and fit 4 in Table 2 (—), back-transformation range $r' = 0.50-3.25$ Å (A); **3**, Fourier transformed range $k = 2-14.9$ Å^{-1}; experimental data (•••) and fit 3 in Table 2 (—), back-transformation range $r' = 0.70-3.50$ Å (B); **4**, Fourier transformed range $k = 2-13.5$ Å^{-1}; experimental data (•••) and fit 5 in Table 2 (—), back-transformation range $r' = 0.50-3.20$ Å (C).

3.1.2. Characterization of 2 in CH_2Cl_2. The spectroscopy of **2** in noncoordinating CH_2Cl_2 solvent is more complex. Resonance Raman spectra (Figure 3B) are indicative of the presence of more than one species. The spectra can be assigned by comparison to spectra of **2-NCMe** (Figure 3A) and the closely related complexes supported by TPA and 6-Me$_3$TPA, which attain limiting low- and high-spin states, respectively, in CH_3CN (Table 1).[36] A weak peak at 789 cm^{-1} in the spectra of **2** was assigned to the ν(O−O) mode of a minor low-spin isomer. The corresponding δ(^{t}Bu) and ν(Fe−O) modes were partially obscured by the δ(^{t}Bu) mode of the high-spin isomer and a CH_2Cl_2 solvent peak, respectively. The remaining features were at frequencies corresponding closely to the ν(Fe−O) and ν(O−O) modes of [Fe^{III}(6-Me$_3$-TPA)(OO^{t}Bu)]$^{2+}$ [36] and were thus assigned to high-spin forms of **2**; the frequencies of these modes reflect weaker peroxide activation relative to the low-spin isomer.[38] The fact that four distinct peaks can be discerned

Table 2. EXAFS Fitting Results for **2-NCPr**, **3**, and **4**[a,b]

		Fe–N/O			Fe–N/O			Fe···C (*Fe···Fe*)			GOF
complex	fit	*n*	*r* (Å)	$\Delta\sigma^2$	*n*	*r* (Å)	$\Delta\sigma^2$	*n*	*r* (Å)	$\Delta\sigma^2$	$\epsilon^2 \times 10^3$ [c]
2-NCPr	1				6	1.97	9.9				1.38
	2	1	1.79	0.9	5	1.99	4.3				1.24
	3	1	1.81	0.8	4	1.99	2.3				1.17
	4	**1**	**1.81**	**0.5**	**4**	**1.99**	**2.3**	**6**	**2.85**	**4.7**	**0.80**
	5	*1*	*1.82*	*0.7*	*4*	*1.99*	*2.2*	*1*	*2.84*	*8.2*	*0.78*
3	1				5	2.03	7.9				1.47
	2	1	1.66	1.5	4	2.01	4.2				1.14
	3	**1**	**1.66**	**1.5**	**4**	**2.01**	**4.1**	**6**	**2.88**	**5.5**	**0.90**
	4	*1*	*1.66*	*1.5*	*4*	*2.01*	*4.2*	*1*	*2.87*	*9.1*	*0.85*
4	1				5	1.93	16				1.47
	2	1	1.79	−2.0	4	1.98	6.3				1.31
	3	2	1.82	1.2	3	2.01	1.9				1.31
	4	1	1.79	−1.9	4	1.98	6.5	6	2.85	3.2	0.79
	5	**2**	**1.82**	**1.2**	**3**	**2.01**	**2.1**	**6**	**2.85**	**3.4**	**0.79**
		(2	1.83	0.5	3	2.02	2.6	6	2.86	5.3)[d]	
	6[e]	*1*	*1.79*	*−1.9*	*4*	*1.98*	*6.3*	*1*	*2.84*	*8.0*	*0.97*
	7	*2*	*1.82*	*1.3*	*3*	*2.01*	*1.9*	*1*	*2.84*	*8.2*	*0.97*

[a] Best fits shown in bold face, alternative outer shell fits to iron shown in italics (see text). [b] Fourier transformed range for **2-NCPr**, $k = 2-15$ Å^{-1} (resolution 0.12 Å); for **3**, $k = 2-14.9$ Å^{-1} (resolution 0.12 Å); and for **4**, $k = 2-13.5$ Å^{-1} (resolution 0.14 Å). r is in units Å; $\Delta\sigma^2$ is in 10^3 Å^2. [c] Back-transformation range for **2-NCPr**, $r' = 0.50-3.25$ Å; for **3**, $r' = 0.70-3.50$ Å; and for **4**, $r' = 0.50-3.20$ Å. [d] While this paper was under review, we obtained additional XAS data on the same sample of **4** at higher resolution ($k = 2-15$ Å^{-1}), which yield a best fit comparable to fit **4**-5. [e] From ref 22.

in the high-spin ν(Fe−O) region and three in the ν(O−O) region suggests that at least two high-spin isomers are present. This was confirmed by varying the excitation wavelength (Figure S3 in Supporting Information), which altered the relative intensities of the various high-spin modes, requiring the presence of distinct LMCT bands. Moreover, the low-spin ν(O−O) mode completely disappeared from spectra with shorter wavelength excitation, consistent with the considerable red shift of the low-spin LMCT band (Figure 1). Additional corroboration of the various assignments was again provided by use of ^{t}Bu^{18}O^{18}OH and $(CD_3)_3$COOH (Table 1 and Figure S4 in the Supporting Information), which induced isotopic shifts of modes comparable to those observed for **2-NCMe** and [Fe^{III}(6-Me$_3$-TPA)(OO^{t}Bu)]$^{2+}$ for the low- and high-spin signals, respectively.[36−38]

The EPR spectrum of **2** also reflected a spin mixture, exhibiting one low-spin iron(III) and two high-spin iron(III) signals (Figure 2B). The features of the low-spin form with $g = (2.21, 2.17, 1.97)$ can be well simulated and account for only 20% of the total spin concentration in the sample. Note that the g_{max} value is at a lower field than those observed for **2-NCPr**, suggesting the replacement of PrCN with an oxygen donor ligand according to the correlation of Talsi for [Fe^{III}(TPA)OOR(X)] species.[39] The only Lewis base present in the CH_2Cl_2 solution that may be strong enough to stabilize a low-spin iron(III) center is excess ^{t}BuOOH, so we suggest that the low-spin EPR signals may arise from the adduct [Fe^{III}(BPMCN)(OO^{t}Bu)(HOO^{t}Bu)]$^{2+}$.

The prominent resonance observed at $g = 4.3$ corresponds to one high-spin species, while a broad feature centered at $g = 8$ probably arises from a distribution of unresolved high-spin species. We employed the following procedure in order to estimate the relative concentrations of the three forms. The $g = 8$ feature was simulated by adding, quite arbitrarily, four $S = 5/2$ spectral components with $D = 1$ cm^{-1} and with E/D values

Table 3. Comparison of Iron(IV) Complexes

complex	$[Fe^{IV}(O)(TMC)(NCMe)]^{2+}$	$[Fe^{IV}(O)(TPA)(NCMe)]^{2+}$	$[Fe^{IV}(O)(N4Py)]^{2+}$	$[Fe^{IV}(O)(\beta\text{-BPMCN})(NCMe)]^{2+}$	$[Fe^{IV}(\beta\text{-BPMCN})(OH)(OO^tBu)]^{2+}$
λ_{max} (nm)	820	724	695	753	650, 845
ϵ (M^{-1} cm^{-1})	400	300	400	280	4000, 3600
XAS pre-edge area	30(4)	30(4)	25(1)	27(1)	12(1) + 7(1)[a]
r(Fe—O) (Å)	1.646(3)[b]	1.65(2)[c]	1.68(2)[c]	1.66(2)[c]	1.82(2)[c]
D (cm^{-1})	28	28	24	24(2)	16(3)
E/D	0[d]	0[d]	0[d,e]	0[d]	0.20(5)
$A_{x,y,z}/g_n\beta_n$ (T)	−25, −20, −3	−23.5, −23.5, −5	−22, −22, −5[e]	−22.5, −18.5, −4.5	−15.5, −21, −6[f,g]
δ (mm/s)	0.17	0.01	−0.04	0.07(1)	0.10(1)
ΔE_Q (mm/s)	1.23	0.93	0.93	1.02(2)	1.76(2)
η	0.5	0.9	0[e]	0.3(3)	0.6
reference	17,18	18,34	19,34	this work	22, this work

[a] Two features observed (see Figure S2 in the Supporting Information). [b] Determined by X-ray diffraction. [c] Determined by EXAFS. [d] E/D can be adjusted between 0 and 0.2 with concomitant adjustment of A_x and A_y; i.e., an increase in E/D has to be accompanied by an increase in A_x and a decrease in A_y. [e] Due to sample impurities of 20%, the low-resolution spectra were fit with a simpler Hamiltonian; the hyperfine tensor was assumed to be axial ($A_x = A_y$), while both E/D and η were set equal to zero. [f] It was necessary to rotate both the A-tensor and the EFG tensor relative to the zero-field splitting tensor. Fits suggested, however, that the principal axis frames of the A- and EFG-tensors were roughly the same; therefore, we kept both tensors in the same frame for the final simulations. The Euler angles (0, 40, 55) rotate the principal frames of the A- and EFG-tensors into the frame of the zero-field splitting tensor. [g] Depending on the D-value and the Euler angles, A_x and A_y can vary substantially. However, $(A_x + A_y)/2g_n\beta_n$ was about −(17−20) T for all reasonable simulations. Euler angle β is roughly 40°, but α and γ can vary considerably.

of 0.18, 0.10, 0.06, and 0.03. The $E/D = 0.18$ subcomponent contributes 60% of the absorption of the $g = 8$ feature, which also contributes to absorption under the $g = 4.3$ feature at 15 K. The result of this simulation is indicated by the red line (Figure 2B). We were not able to simulate the tails of the g = 4.3 feature with sufficient accuracy, so the spin concentration of this species was determined by integration of the spectrum after removing the contribution of the simulated $g = 8$ species. Double integration of the $g = 4.3$ signal, taking into account the g-value correction according to Aasa,[45] yielded the spin concentration of the $g = 4.3$ Kramers doublet. The total spin concentration of this species was then obtained by assuming that the $g = 4.3$ doublet is populated to ca. 33% at 15 K; this assumption is reasonable for $D < 1.5$ cm^{-1}, and reported D-values of high-spin peroxo complexes are ca. 1 cm^{-1}.[40] Using these procedures, we obtained the following spin concentrations and mole percentages for the three species: low-spin form, 0.18(2) mM, 21%; $g = 4.3$ species, 0.27(4) mM, 32%; $g = 8$ species, 0.40(8) mM, 47%. A similar distribution of the three species was observed for two other samples.

The multiplicity of EPR signals observed for **2** in CH_2Cl_2 raises the question of whether they all arise from alkylperoxoiron(III) species. If all the iron present in the sample were assumed to contribute to the charge-transfer band at 560 nm, the calculated molar extinction coefficient would be 2500 M^{-1} cm^{-1}. This value is comparable to those observed for other Fe^{III}−OOR complexes (2000−2200 M^{-1} cm^{-1}),[36,46,47] whether high-spin or low-spin, suggesting that all observed EPR species are Fe^{III}−OOR intermediates. Excluding either one of the high-spin EPR species yields an unprecedented molar extinction coefficient of at least 3300 M^{-1} cm^{-1}. We do not know at present what structural differences at the high-spin centers give rise to this distribution of E/D values, which is frequently observed for high-spin iron(III). Possible formulations include $[Fe^{III}(BPMCN)(OO^tBu)(HOO^tBu)]^{2+}$, in equilibrium with its postulated low-spin form, and $[Fe^{III}(BPMCN)(OO^tBu)(OTf)]^+$; a sixth ligand could also be absent, allowing the resulting five-coordinate metal center to adopt a range of geometrical arrangements. Unfortunately, due to the opacity of the solvent to 6−14-KeV X-rays, neither Mössbauer nor XAS spectra of **2** could be obtained in CH_2Cl_2 to corroborate the conclusions drawn from the Raman and EPR data.

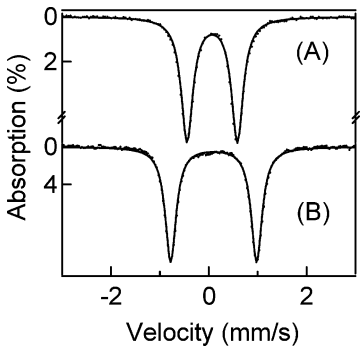

Figure 6. Mössbauer spectra of **3** (A) and **4** (B) recorded at 4.2 K in zero field. Solid lines are spectral simulations using the ΔE_Q and δ values listed in Table 3.

3.2. Conversion of 2-NCMe to an Oxoiron(IV) Species 3. Decay of **2-NCMe** over a period of 1 h in CH_3CN solution at −45 °C afforded a pale green chromophore **3** ($\lambda_{max} = 753$ nm, $\epsilon = 280$ M^{-1} cm^{-1}, Figure 1A) resembling those of authenticated oxoiron(IV) complexes (Table 3).[17−19] Consistent with assignment of this chromophore to ligand field transitions,[23] attempts to observe a ν(Fe═O) mode by resonance Raman spectroscopy using laser excitation into the optical bands were unsuccessful. (A Raman mode was observed at 752 cm^{-1} using 752.5-nm excitation of an iron(IV) species obtained by hypobromite oxidation of [Fe(Me-TPPN)(Cl)](PF_6) in 2:1 MeOH/acetone solution, was assigned as an iron(IV)−oxygen stretch, but was not shifted by ^{18}O isotope labeling of the oxidant.[20])

A Mössbauer study of ^{57}Fe-enriched **3** prepared at −25 °C was performed in order to confirm the oxidation state of the iron center; two representative spectra of **3** are shown (Figures 6A, 7A). At 4.2 K, the zero-field Mössbauer spectrum of **3** exhibits a quadrupole doublet with $\Delta E_Q = 1.02(2)$ mm/s and $\delta = 0.07(1)$ mm/s that represents ca. 90% of the total iron in the sample (Figure 6A). In strong applied fields, **3** behaved like an $S = 1$ paramagnet (Figure 7A and Figure S5 in the Supporting Information).

(45) Aasa, R.; Vanngard, T. *J. Magn. Reson.* **1975**, *17*, 308−315.
(46) Ménage, S.; Wilkinson, E. C.; Que, L., Jr.; Fontecave, M. *Angew. Chem., Int. Ed. Engl.* **1995**, *34*, 203−205.
(47) Wada, A.; Ogo, S.; Watanabe, Y.; Mukai, M.; Kitagawa, T.; Jitsukawa, K.; Masuda, H.; Einaga, H. *Inorg. Chem.* **1999**, *38*, 3592−3593.

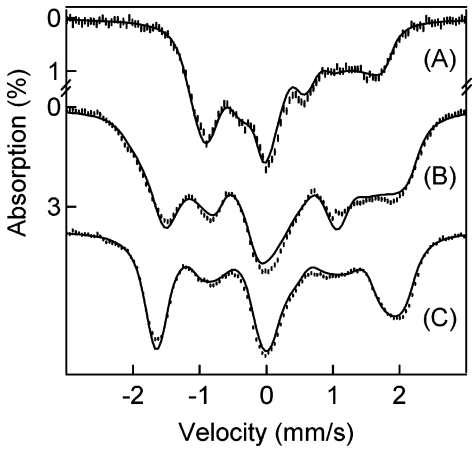

Figure 7. 4.2 K Mössbauer spectra recorded in an 8 T magnetic field applied parallel to the observed γ-radiation of **3** at 4.2 K (A) and **4** at 4.2 K (B) and **4** at 100 K (C). Solid lines are spectral simulations based on eq 1 using the parameters listed in Table 3.

The parameters for **3** (Table 3) were obtained by fitting the spectra to the $S = 1$ spin Hamiltonian

$$\mathscr{H} = D\left[\hat{S}_z^2 - \frac{1}{3}S(S+1)\right] + E(\hat{S}_x^2 - \hat{S}_y^2) + \beta\hat{\mathbf{S}}\cdot\mathbf{g}\cdot\mathbf{B} + \hat{\mathbf{S}}\cdot\mathbf{A}\cdot\hat{\mathbf{I}} - g_n\beta_n\hat{\mathbf{I}}\cdot\mathbf{B} + \mathscr{H}_Q \quad (1)$$

$$\mathscr{H}_Q = \frac{eQV_{zz}}{12}\left[3\hat{I}_z^2 - \frac{15}{4} + \eta(\hat{I}_x^2 - \hat{I}_y^2)\right] \quad (2)$$

All parameters in eqs 1 and 2 have their conventional meanings. For all simulations for **3** (and **4** below) we have used $g_x = g_y = g_z = 2.0$ (see comment in section 3.3.5). For **3** the parameter E/D can be chosen anywhere between 0 and 0.2, provided that the x and y components of the magnetic hyperfine tensor, A_x and A_y, are adjusted to produce the same distribution of the magnetic hyperfine field in the $x-y$ plane (see footnote in Table 3). These parameters compare well with those of the crystallographically characterized $[Fe^{IV}(O)(TMC)(NCCH_3)]^{2+}$ and other recently characterized oxoiron(IV) complexes (Table 3). Further discussion of the Mössbauer spectra of **3** can be found in section 3.3.5 (vide infra) in regard to spectral features that apply to all iron(IV) complexes listed in Table 3.

X-ray absorption spectroscopy confirmed the formulation of **3** as an oxoiron(IV) complex. The Fe K-edge shifts to 7124.6 eV, a 0.5-eV increase relative to that of **2-NCPr**. This small shift has been observed between alkylperoxoiron(III) and oxoiron(IV) complexes of TPA and N4Py and can be ascribed to the increased covalency of the Fe^{IV}═O bond.[34] A relatively sharp 1s→3d transition was observed at 7114.2 eV in the pre-edge region with an intensity of 27(1) units (Figure 4A); this large value is indicative of a significant distortion away from a centrosymmetric environment and is comparable to those found for other mononuclear oxoiron(IV) complexes with either porphyrin[48,49] or nonheme supporting ligands.[18,34] The EXAFS region (Figures 4B, 5B) was best fit with three shells of scatterers: one O atom at 1.66 Å associated with the terminal Fe═O bond, four N atoms at 2.01 Å corresponding to the donor atoms of the tetradentate BPMCN ligand, and an outer shell of 6 C atoms from the ligand at 2.88 Å (fit **3**-3, Table 2 and Table S2 in the Supporting Information). A second sample gave similar fitting results (Table S3 and Figures S6 and S7 in Supporting Information). Thus, the accumulated spectroscopic information supports the conclusion that the decay of **2-NCMe** produces an oxoiron(IV) complex **3** in high yield.

3.3. Conversion of 2 in CH_2Cl_2 to a Distinct Iron(IV) Species 4. In contrast to the precedented results obtained for the decay of **2-NCMe**, the decay of **2** in CH_2Cl_2 yielded an iron(IV) complex **4**,[22] which is distinct from the subsequently discovered oxoiron(IV) complexes.[17−19] Turquoise blue crystals of **4** were isolated as small feathery plates from CH_2Cl_2 by diffusion of pentane over 1−2 months at −90 °C, and with care these could be redissolved without decomposition into cold CH_2Cl_2, MeOH, or butyronitrile. Because the isolated solid samples of **4** were not adequate for X-ray diffraction studies, a structural formulation can only be based on indirect, primarily spectroscopic methods. Evidence for a low-spin iron(IV) center was unequivocally revealed by Mössbauer spectroscopy (Table 3), but its quadrupole splitting was significantly larger than those of **3** and other oxoiron(IV) complexes (Table 3). Even more obviously different were the intense low-energy absorption bands of **4** at 656 and 845 nm ($\epsilon = 4000$ and 3600 M^{-1} cm^{-1}, respectively, Figure 1B) that impart its characteristic color;[22] these bands almost certainly arise from charge-transfer transitions, in contrast to the much weaker ligand field transitions associated with pale green **3** and related complexes.[23] The visible−NIR spectrum of **4** was essentially identical in the range of solvents described above. Laser excitation into the CT bands resulted in the observation of resonance-enhanced Raman ν(Fe−O) modes not observed thus far for the oxoiron(IV) complexes[22] and lying at lower energies than expected for a terminal Fe^{IV}═O bond.[17,50] XAS analysis of both the pre-edge and EXAFS regions argued against the presence of a terminal oxo ligand on **4** (Tables 2, 3). The previously reported elemental analysis of thermally decomposed **4** afforded an Fe/N/S/F atom ratio of 1.00:3.94:1.95:5.97 in the decomposed material (Table S5 in the Supporting Information),[22] unequivocally demonstrating the presence of one iron, one BPMCN ligand, and two triflate ions in **4**, since these elements can neither be introduced by organic contaminants nor be lost by decomposition to volatile coproducts. While this application of elemental analysis is obviously less than ideal, it nonetheless successfully establishes experimental mole ratios of ligand and counterions to iron in **4**. Taken together with the spectroscopic data, these results point to a generic formulation of **4** as $[Fe^{IV}(BPMCN)(X)(Y)](OTf)_2$, where X and Y are undefined O/N-donor ligands with a combined dianionic charge. Since the EXAFS data were similar to those of crystallographically characterized $[Fe_2(\mu\text{-}O)_2(5\text{-}Et_3TPA)_2]^{3+}$,[16] the analysis for **4** could be interpreted to indicate the presence of an iron scatterer at 2.81 Å, suggesting that it had an $Fe_2(\mu\text{-}O)_2$ core structure as well. Based on this initial EXAFS and Raman analysis, and consistent with the generic formula just given, **4** was formulated as $[Fe^{IV}_2(\mu\text{-}O)_2(BPMCN)_2](OTf)_4$, the dimeric form of **3**.[22] This conclusion has been reconsidered in the present study, as described below.

3.3.1. EXAFS Analysis of 4 Revisited. The best fits to the inner-sphere EXAFS data of **4** consisted of 1−2 N/O scatterer(s) at ca. 1.8 Å and 3−4 N/O scatterers at ca. 2.0 Å, while

(48) Wolter, T.; Meyer-Klaucke, W.; Müther, M.; Mandon, D.; Winkler, H.; Trautwein, A. X.; Weiss, R. *J. Inorg. Biochem.* **2000**, *78*, 117−122.
(49) Nam, W.; Choi, S. K.; Lim, M. H.; Rohde, J.-U.; Kim, I.; Kim, J.; Kim, C.; Que, L., Jr. *Angew. Chem., Int. Ed.* **2003**, *42*, 109−111.
(50) Kitagawa, T.; Mizutani, Y. *Coord. Chem. Rev.* **1994**, *135/136*, 685−735.

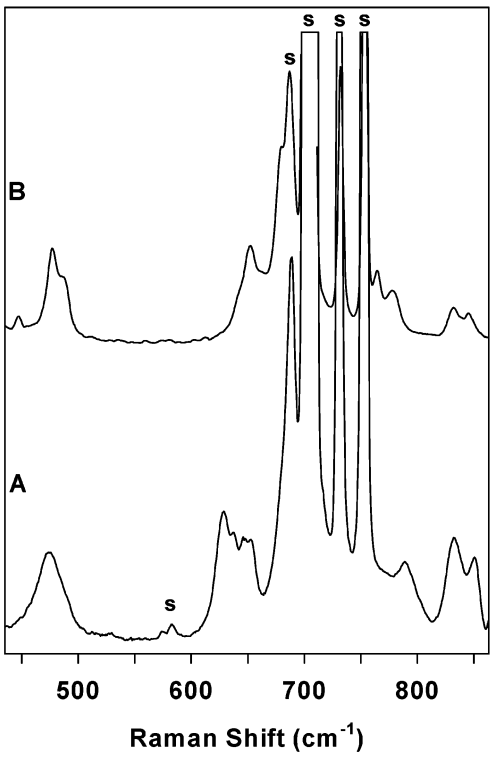

Figure 8. Comparison of Raman spectra recorded using 632.8-nm laser excitation of frozen aliquots from a CH_2Cl_2 reaction solution that span the conversion of **2** (A) to **4** (B).

the large outer-sphere peak at $r' \sim 2.4$ Å fit well to an Fe scatterer, consistent with the proposal for an $Fe_2(\mu\text{-}O)_2$ diamond core structure for **4** (Figure 5C, Table 2, and Table S4 in the Supporting Information).[22] However, EXAFS spectra subsequently obtained on **2-NCPr** and **3** also exhibited large peaks at $r' \sim 2.4$ Å (Figures 4B and 5A, B), notwithstanding their obvious mononuclear character, that were fit well with a shell of the six carbon atoms adjacent to the ligating nitrogen atoms of the BPMCN ligand. This feature is more intense relative to the related TPA and N4Py complexes,[34,40] presumably because the relevant iron−carbon distances in BPMCN complexes fall within a particularly narrow range and include two carbon atoms on the unique cyclohexyl backbone.[44] The outer-sphere features observed for **2-NCPr** and **3** could also be fit to an iron scatterer (Table 2, fits **2**-5 and **3**-4, respectively), and conversely, the data for **4** could alternatively accommodate a shell of carbon scatterers (fit **4**-5, Table 2). The resulting ambiguity cast doubt on the Fe_2O_2 diamond core structure proposed earlier and compelled a re-examination of the Raman and Mössbauer data cited in support of this conclusion.

3.3.2. Raman Spectroscopy of 4 Revisited: 4 is an Alkylperoxo Complex. As previously reported,[22] the spectrum of **4** is dominated by intense features at 653, 680, and 687 cm^{-1} (Figures 8−10). A 23−26 cm^{-1} downshift in these features observed in a spectrum of **4** prepared with $^tBu^{16}O^{18}OH$ led to their assignment as vibrations with dominant ν(Fe−O) character (Figure 9C), for which Hooke's Law predicts a 30 cm^{-1} shift. Preparation of **4** using a 1:1 mixture of $^tBu^{16}O^{16}OH$ and $^tBu^{16}O^{18}OH$ was shown to give features in addition to those of the limiting isotopomer peaks, and it was suggested that these were associated with coupled modes of an $Fe_2(\mu\text{-}^{16}O)(\mu\text{-}^{18}O)$ diamond core,[22] although the relative intensities of the additional

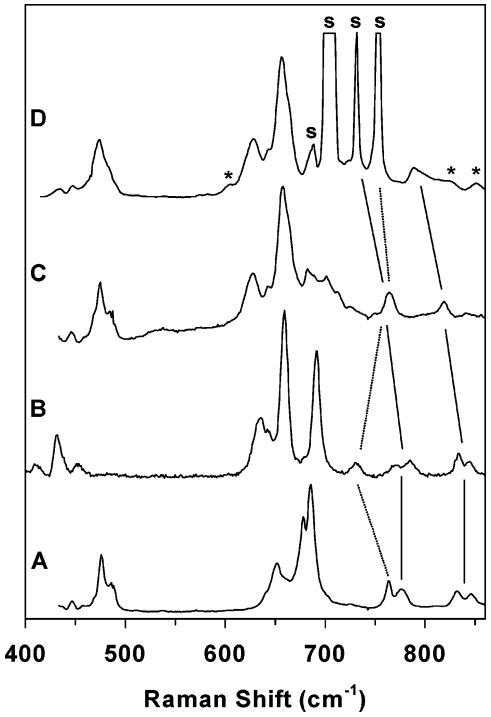

Figure 9. Resonance Raman spectra of **4** generated with normal ^{t}BuOOH (A), $(CD_3)_3COOH$ (B), $^tBu^{16}O^{18}OH$ (C), and $^tBu^{18}O^{18}OH$ (D). Spectra A−C were obtained in frozen MeOH, and spectrum D was obtained in frozen CH_2Cl_2 ("s" denotes solvent resonances); spectra A and C were obtained with 632.8-nm laser excitations, and spectra B and D with 647.1-nm excitations. Isotope shifts of the ν(O−O) and $\nu(^t$Bu−O) modes are highlighted by solid and dashed lines, respectively; asterisks in spectrum D denote features that can be assigned to residual **2**.

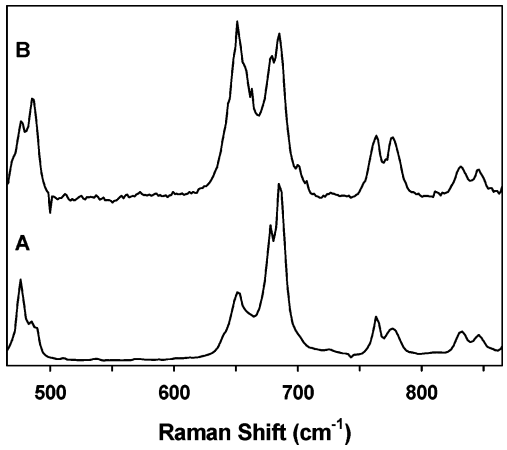

Figure 10. Resonance Raman spectra of **4** recorded in frozen MeOH using 632.8-nm (A) and 752.5-nm (B) laser excitation.

"mixed isotope" features were significantly weaker than implied by the statistical distribution.

Additional and previously unreported peaks were also observed in Raman spectra of **4**; these are comparable to $\delta(^t$Bu) and ν(O−O) modes of alkylperoxoiron(III) complexes (Figure 8). The latter features are less intense relative to the dominant new ν(Fe−O) modes (Figure 8B), perhaps leading to their casual attribution to residual **2** (Figure 8A). Close scrutiny of the spectra reveals that this is not the case, suggesting that **4** is also an alkylperoxo complex. A complete isotope labeling study of the Raman features of **4** was accordingly carried out by preparing samples using $(CD_3)_3COOH$ and $^tBu^{18}O^{18}OH$ (Figure 9B and D, Table 1). Significantly, the use of the d_9-isotopomer

induced shifts of the previously reported ν(Fe−O) modes, demonstrating these modes are coupled to *tert*-butyl deformations and thus clearly excluding an $Fe_2(\mu\text{-}O)_2$ core structure. There must be an intact alkylperoxo ligand on **4**, and given the prior Mössbauer assignment of an iron(IV) oxidation state (vide infra),[22] **4** thus appears to be a novel alkylperoxoiron(IV) complex.

The isotope shift patterns observed for **4** are reported and compared with those found for corresponding alkylperoxoiron(III) complexes in Table 1. Bands at 478 and 487 cm^{-1} (Figure 9A) were downshifted 48−50 cm^{-1} upon deuterium substitution (Figure 9B), but not by ^{18}O (Figure 9C, D), and accordingly were assigned to vibrations with predominant $\delta(^tBu)$ character. Bands at 776, 832, and 846 cm^{-1} were not shifted by deuterium substitution but downshifted in the $^tBu^{16}O^{18}OH$ product spectra by 21−23 cm^{-1}. The latter two peaks also downshifted 44−48 cm^{-1} with use of $^tBu^{18}O^{18}OH$. The ^{18}O isotope shifts closely approach their Hooke's Law limits for pure ν(O−O) modes. A unique mode at 765 cm^{-1} (Figure 9A, C) was not perturbed in the $^tBu^{16}O^{18}OH$ product spectrum but was downshifted by the other two isotopic substitutions; this behavior and the observed frequency allow for its assignment as a $\nu(^tBu\text{−}O)$ mode. The features just below 700 cm^{-1} discussed earlier were downshifted by essentially identical values using $^tBu^{16}O^{18}OH$ and $^tBu^{18}O^{18}$-OH, as expected from their assignment as predominantly ν-(Fe−O) modes coupled to *tert*-butyl deformations.

The considerable degree of decoupling of the ν(O−O) modes implied by the large shifts induced by ^{18}O substitution and the corresponding lack of a deuterium labeling effect probably accounts for their relatively weak resonance enhancement, and distinguishes **4** from alkylperoxoiron(III) complexes (Table 1 and Figure 9D). However, the resonance Raman spectrum of **4**, unlike that of low-spin **2-NCMe**, also clearly exhibited two distinct sets of $\delta(^tBu)$, ν(Fe−O), and ν(O−O) vibrations, suggestive of the presence of more than one isomer. When the laser excitation was shifted from 632.8 to 752.5 nm, the relative intensities of various peaks changed to reveal two distinct sets of alkylperoxo modes, one set with bands at 477, 687, 832, and 845 cm^{-1} and the second at 487, 652, and 778 cm^{-1} that were more enhanced with 752.5-nm excitation (Figure 10). The two sets of Raman modes provide evidence of two isomers with distinct charge-transfer transitions and Raman features.

Raman spectra of **4** prepared using 1:1 mixtures of $^tBuOOH/(CD_3)_3COOH$ and $^tBu^{16}O^{16}OH/^tBu^{18}O^{18}OH$ were also recorded directly from frozen reaction solutions in CH_2Cl_2, and in both cases, the observed spectra were simple superpositions of limiting isotopic spectra. There was no evidence for the complexity analogous to that previously reported in the spectrum of **4** derived from $^tBu^{16}O^{16}OH/^tBu^{16}O^{18}OH$, which was attributed to the presence of coupled, mixed isotope bands. Given our better current understanding of the reaction of **1** with ^tBuOOH, we suspect that the added complexity of the earlier report might be ascribed to the CH_3CN that served as the solvent for the $^tBu^{16}O^{18}OH$ stock, which can bind to the iron(III) center of **2** and stabilize it, possibly giving rise to extra features from residual **2-NCMe**.

3.3.3. ^2H NMR Characterization of 4. The investigation of **4** was extended to obtain independent evidence for the composition and isomerism by NMR spectroscopy (Figure 11). Reaction of **1** (5.1 mM) with $(CD_3)_3COOH$ (23.6 mM) in CH_2Cl_2 at −67 °C gave a solution of labeled **4** after standing for 2 h. A ^2H (deuterium) NMR spectrum recorded in a precooled probe at −77 °C revealed two signals at 1.1 (fwhm ≈ 40 Hz) and −21.0 ppm (fwhm ≈ 100 Hz) in a 4:1 area ratio (Figure 11). The more intense peak in the diamagnetic region represents the unresolved resonances of excess $(CD_3)_3COOH$ and its reduction product(s), while the upfield shifted signal can be assigned to a d_9-alkylperoxo ligand coordinated to a paramagnetic metal center. For comparison, a ^2H NMR signal at −4.2 ppm was reported at −52 °C for the $S = {}^1/_2$ alkylperoxoiron(III) complex of the related TPA ligand;[39] the larger shift observed for **4** is consistent with the higher spin state.[51] Unfortunately, attempts to observe corresponding signals of **2** in CH_2Cl_2 and CH_3CN were not successful.

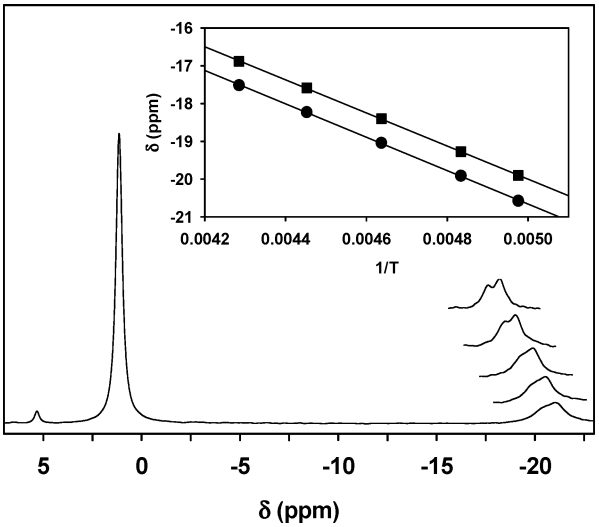

Figure 11. ^2H NMR spectrum in CH_2Cl_2 at 196 K (full trace) of reaction products of **1** (5.1 mM) with $(CD_3)_3COOH$ (23.6 mM), plus excerpts recorded with increasing temperature. Inset illustrates correlation of paramagnetic shifts with inverse temperature; least-squares regressions are shown with formula $\delta = -4380(27)T^{-1} + 1.90(13)$ (minor component, $R^2 = 0.9999$) and $\delta = -4423(36)T^{-1} + 1.45(17)$ (major component, $R^2 = 0.9998$).

The paramagnetically shifted ^2H signal of **4** observed at −77 °C was asymmetric. As the temperature was raised, the feature sharpened, and two distinct resonances were clearly resolved (Figure 11), corroborating the isomerism suggested by the wavelength-dependent Raman data. A 60:40 intensity ratio was determined by least-squares fitting of two Lorentzian peaks with equal widths. As expected for Curie Law behavior,[51] the paramagnetic shifts of the two resonances were found to be inversely proportional to temperature (Figure 11 inset), and extrapolation to infinite temperature yielded limiting shifts of 1.9 and 1.4 ppm for the *tert*-butyl resonances.

Integration of the observed peaks against the natural abundance solvent ^2H resonance at 5.3 ppm, or equivalently against a known amount of added $CDCl_3$, gave normalized concentration estimates of 19.4 and 4.8 mM, respectively, accounting for all the added $(CD_3)_3COOH$ (23.6 mM); **4** must be a monoalkylperoxo complex formed as a mixture of two isomers in 94(3)% spectroscopic yield. The yield of **4** produced by addition of varying stoichiometric ratios of $(CD_3)_3COOH$ to **1** was also determined by ^2H NMR spectroscopy (Figure 12). The

(51) Ming, L.-J. In *Physical Methods in Bioinorganic Chemistry*; Que, L., Jr., Ed.; University Science Books: Sausalito, CA, 2000; Chapter 8.

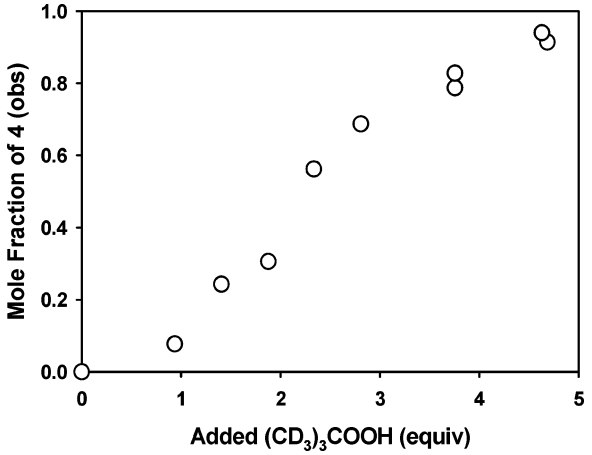

Figure 12. Titration series illustrating the yield of **4** as a function of added $(CD_3)_3COOH$ to **1** as determined by ^2H NMR spectroscopy. Amounts of **4** were quantified by integrating the intensities of the paramagnetically shifted $(CD_3)_3C-$ resonances against that of $CHDCl_2$ at natural abundance in the solvent.

data indicate that consumption of 5 equiv of ^{t}BuOOH is required to obtain nearly stoichiometric accumulation of **4**. The formation of any alkylperoxoiron(IV) complex from **1** would minimally require 2 equiv of ^{t}BuOOH (eq 3), so other pathways must exist that consume additional ^{t}BuOOH, such as that leading through intermediate **2** and its subsequent O−O bond homolysis to release ^{t}BuO$^\bullet$ (Scheme 1), which can readily react with excess ^{t}BuOOH.

$$[Fe^{II}(\beta\text{-BPMCN})]^{2+} + 2\ {}^t\text{BuOOH} \rightarrow [Fe^{IV}(\beta\text{-BPMCN})(OO{}^t\text{Bu})]^{3+} + {}^t\text{BuOH} + OH^- \quad (3)$$

3.3.4. Mössbauer Analysis of 4 Updated. Representative Mössbauer spectra of **4** are shown in Figures 6B and 7B,C (additional spectra are shown in Figure S8 in the Supporting Information). The spectra were the same for polycrystalline solids and frozen butyronitrile solutions. In our earlier report,[22] we concluded that the spectra of **4** could be fit well to an $S = 1$ spin Hamiltonian of a *mononuclear* iron(IV) complex. However, due to our initial interpretation of the resonance Raman and EXAFS data suggesting an $Fe_2(\mu\text{-}O)_2$ core for **4**, we found that the Mössbauer spectra could also be fit to a spin-coupled iron(IV) dimer ($\mathscr{H} = JS_1 \cdot S_2$; $S_1 = S_2 = 1$), provided that |J| was (somewhat implausibly) smaller than 5 cm^{-1}. While our previous analysis could not distinguish between a monoiron(IV) and a weakly coupled diiron(IV) complex containing symmetric $S = 1$ sites, it excluded the possibility of high-spin ($S = 2$) iron(IV) for **4**. This analysis remains valid, but the data can now be viewed in a somewhat different light given the different structure assigned to **4** (vide infra) and the Mössbauer characterization of several nonheme oxoiron(IV) complexes synthesized since our 2001 paper.[17−19]

The low-field Mössbauer spectrum of **4** unequivocally establishes the ΔE_Q and δ values for the iron(IV) center, but the high-field data can be fit with *D*- and *A*-values having a range wider than those found for related oxoiron(IV) complexes (Table 3). Furthermore, as reported earlier[22] and unlike the case for the oxoiron(IV) complexes, the metal center must have less than rhombic symmetry, as evidenced by the requirement that the electric field gradient (EFG) and the A-tensor had to be rotated relative to the zero-field splitting (ZFS) tensor. This result is plausible as the mixed ligand environment of the iron(IV) site of **4** does indeed suggest low symmetry. Alternatively, the complexity may arise from the presence of more than one iron(IV) component. The Raman and NMR data presented in the present work provide evidence for the presence of two geometric isomers (vide supra). While these geometric isomers do not appear to give rise to distinct zero-field Mössbauer spectra (they have the same ΔE_Q and δ to within ±0.02 mm/s and ±0.01 mm/s, respectively), they may afford different high-field spectra that account for at least some of the large variations in *D*, A_x, and A_y values allowed by the fits.

All iron(IV) complexes listed in Table 3 have large *D*-values, but the *D*-value of **4** is somewhat smaller than those of the oxoiron(IV) complexes. In the frequently used $(t_{2g})^4$ ($S = 1$) crystal field model of Oosterhuis and Lang,[52] a large zero-field splitting parameter *D* implies substantial unquenching of orbital angular momentum, leading to a decrease in the magnitude of A_x and A_y (see Figure 3 of ref 52). This unquenching is caused by spin−orbit mixing of excited $S = 1$ manifolds associated with excited orbital states into the $S = 1$ ground triplet. In the Oosterhuis−Lang model, a *D*-value of 25 cm^{-1} would suggest low-lying orbital states (d_{xz}, d_{yz} in a coordinate system for which d_{xy} is the ground state in the crystal field; see ref 52) around 1600 cm^{-1}. This mixing would add a sizable (positive) orbital contribution to the *A*-tensor, and for $D = 25$ cm^{-1} one would expect A_x and A_y to be ca. −10 T, in stark contrast to the experimental data listed in Table 2. Decker and co-workers have recently published low-temperature optical and MCD studies of $[Fe^{IV}(O)(TMC)(NCCH_3)]^{2+}$,[23] the complex listed in the first column of Table 3. These studies reveal that the lowest excited $S = 1$ states (associated with $d_{xz,yz}$) are ca. 10 500 cm^{-1} above the d_{xy} ground state. For these orbital spacings the *D*-values of the iron(IV) site would be ∼4 cm^{-1} according to the Oosterhuis−Lang model.

Neese and Solomon have shown that spin−orbit mixing between $S = 2$ and $S = 1$ states contributes in second order to the zero-field splitting of the $S = 1$ ground triplet.[53] Such mixing can dramatically increase *D* but has no effect on the *g*-tensor[53,54] or the *A*-tensor.[54] For $[Fe^{IV}(O)(TMC)(NCCH_3)]^{2+}$, DFT calculations by Decker et al. suggest a low-lying $S = 2$ configuration at 4500 cm^{-1},[23] and very recently, Schöneboom, Neese, and Thiel have shown that the large zero-field splitting of this complex can indeed be attributed to such mixing.[55] That study also shows, as expected, that the *g*-values of $[Fe^{IV}(O)(TMC)(NCCH_3)]^{2+}$, which are not affected by mixing with the $S = 2$ state, are close to $g = 2.0$, and for this reason we have fitted the data of **3** and **4** by fixing the *g*-values to $g = 2.0$.

The low symmetry of **4** and the preceding discussion suggest a careful approach for the analysis guided by theory such as DFT calculations. In our experience, DFT calculations often provide good estimates of the magnitude and orientation of the spin-dipolar part of the *A*-tensor;[54] moreover, such calculations can provide guidance regarding a low-lying $S = 2$ configuration.[23] Extensive DFT studies of **4** and of simplified models in our laboratory showed that the complex has indeed a low-lying

(52) Oosterhuis, W. T.; Lang, G. *J. Chem. Phys.* **1973**, *58*, 4757−4765.
(53) Neese, F.; Solomon, E. I. *Inorg. Chem.* **1998**, *37*, 6568−6582.
(54) Vrajmasu, V.; Bominaar, E.; Meyer, J.; Münck, E. *Inorg. Chem.* **2002**, *41*, 6358−6371.
(55) Schöneboom, J. C.; Neese, F.; Thiel, W. *J. Am. Chem. Soc.* **2005**, *127*, 5840−5853.

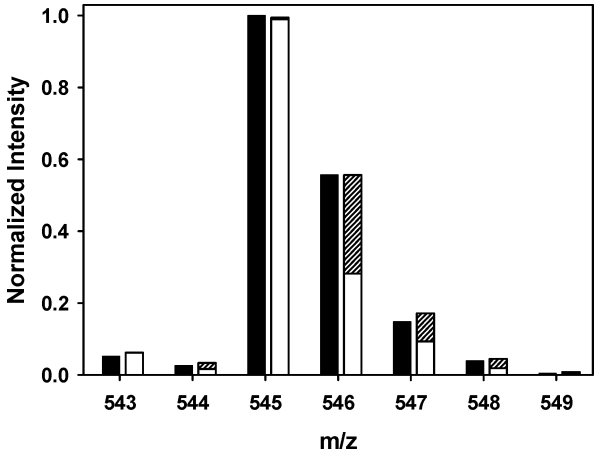

Figure 13. Parent ion observed by electrospray mass spectrometry of **4** redissolved in PrCN. Dark bars are observed intensities; open bars are the calculated isotopic mass distribution of $[Fe^{IV}(O)(BPMCN)(OTf)]^+$ stacked with the overlapping mass distribution of $[Fe^{III}(OH)(BPMCN)(OTf)]^+$ (0.28 equiv, shaded bars).

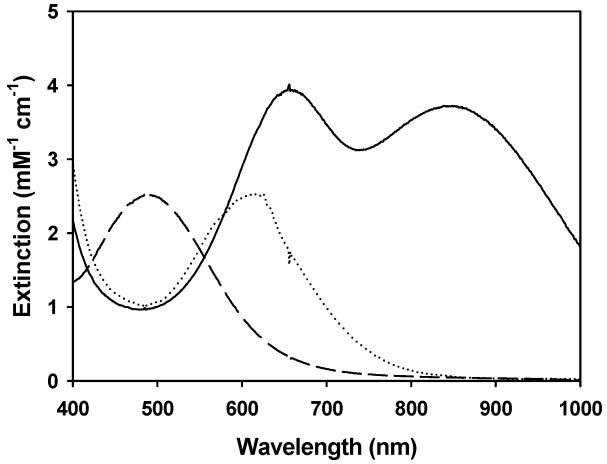

Figure 14. Visible−NIR spectra of **4** in CH_2Cl_2 solution at −65 °C (solid line), the product chromophore produced by addition of ferrocene to **4** in PrCN to form **2-NCPr** (···), distortion of the charge transfer band presumably results from overlapping absorption of the blue ferrocenium byproduct),[56] and that of **2-OH** (- - -), formed by NEt_3 addition to **4** in CH_2Cl_2.

$S = 2$ state. However, these studies revealed also that the quadrupole splitting of **4** depends very critically on geometrical variations (such as rotation of the presumed OH^- ligand around the Fe−O axis) that affect the ground state energy only in a minor way. These observations suggest that solvent or crystal packing effects may be important. These matters, which exceed our present computational capabilities, are under further consideration.

3.3.5. Reformulation of 4. The reinterpreted and extended spectroscopic investigation presented above now clearly demonstrates that **4** is a monomeric alkylperoxoiron(IV) complex closely related to the oxoiron(IV) complex **3**. The remaining uncertainty in a complete and correct formulation of **4** lies with the identity of the sixth ligand necessary to obtain octahedral coordination of the metal ion along with the alkylperoxide and tetradentate BPMCN ligands. Given the generic formulation of **4** as $[Fe^{IV}(BPMCN)(X)(Y)](OTf)_2$ and the established presence of an anionic alkylperoxo ligand, the single remaining ligand must be a monoanionic O/N-donor. Moreover, the sixth site ligand probably accepts the proton balance generated by the alkylperoxide ligation. Since the EXAFS analysis of **4** shows the absence of a short (ca. 1.65 Å) Fe═O bond and provides evidence for one or two longer (ca. 1.82 Å) Fe−O/N bonds (Table 2), we propose the sixth ligand to be hydroxide and thus reformulate **4** as $[Fe^{IV}(BPMCN)(OH)(OO^tBu)](OTf)_2$. Additional experiments, described below, also support the designation of hydroxide as the sixth ligand.

Electrospray ionization mass spectral analysis of **4** was carried out on samples from either a CH_2Cl_2 reaction solution or the isolated product redissolved in butyronitrile. In either case, the only iron(IV) species observed was a monocation at $m/z = 545$, corresponding to $[Fe^{IV}(O)(BPMCN)(OTf)]^+$ (Figure 13; full spectra are shown in Figures S9 and S10 in the Supporting Information). The observed species could be generated by facile loss of neutral ^{t}BuOOH from **4**. Additional ions were also observed corresponding to reduced species including $[Fe^{III}(BPMCN)(OH)(OTf)]^+$ (m/z 546), which is consistent with the loss of a ^{t}BuOO$^\bullet$ radical fragment, a known decomposition pathway. Thus, the mass spectral results are consistent with a formulation of **4** as $[Fe^{IV}(BPMCN)(OH)(OO^tBu)](OTf)_2$.

The possibility of one-electron reduction of **4** to form alkylperoxoiron(III) complexes (Scheme 1) was explored to test the formulation as $[Fe^{IV}(BPMCN)(OH)(OO^tBu)]^{2+}$. These experiments were carried out at −65 °C with **4** either generated in situ in CH_2Cl_2 or isolated and redissolved in PrCN (i.e., in the absence of excess ^{t}BuOOH). Treatment of **4** in PrCN with 1 equiv of ferrocene resulted in immediate conversion to a species that exhibited a λ_{max} near 600 nm (Figure 14). An EPR spectrum of the product consisted of two overlapping $S = {}^1/_2$ signals in a nearly 1:1 ratio that were coincident with the signals of **2-NCPr** (vide supra). The conversion to low-spin iron(III) species was confirmed by a Mössbauer experiment. The facile conversion of **4** to **2-NCPr** apparently entails rapid reduction of iron(IV) to iron(III), as expected for a one-electron outer-sphere transfer process with sufficient thermodynamic driving force, followed by displacement of a labile sixth ligand with solvent to form the low-spin alkylperoxoiron(III) complex.

In contrast, one-electron reductions of **4** in CH_2Cl_2 afforded *high-spin* alkylperoxoiron(III) species, as indicated by Raman spectra that are similar to but simpler than the spectrum of **2** (Figure 15). Addition of 1 equiv of ^{n}Bu$_3$SnH to **4** at −65 °C resulted in its slow conversion to a violet chromophore ($\lambda_{max} = 526$ nm) over 2 h, which in turn was immediately converted to an orange species with λ_{max} at 490 nm ($\epsilon = 2500\ M^{-1}\ cm^{-1}$, Figure 14) upon treatment with base. The latter is identical to the chromophore formed instantaneously in CH_2Cl_2 by treating **2** with 2,6-lutidine. We thus formulate the violet chromophore as $[Fe^{III}(BPMCN)(OH_2)(OOR)]^{2+}$ (**2-OH$_2$**), the result of a hydrogen-atom transfer to **4**, and the orange chromophore as $[Fe^{III}(BPMCN)(OH)(OOR)]^+$ (**2-OH**), the conjugate base of **2-OH$_2$** (Scheme 1). The use of 1 equiv of ferrocene as a reductant in CH_2Cl_2 also rapidly elicited a similar chromophore ($\lambda_{max} = 505$ nm) upon mixing.

Complex **4** was also treated with bases in CH_2Cl_2 in an attempt to deprotonate the postulated hydroxyl group to give an oxoiron(IV) complex. While 2,6-lutidine had no effect on the spectrum of **4**, addition of excess NEt_3 also converted **4** to the orange chromophore discussed above (Figure 14), but this reaction required 15 min. The slow rate of reaction is consistent with NEt_3 also acting as a one-electron reductant rather than simply as a base.[57] Essentially identical Raman spectra were

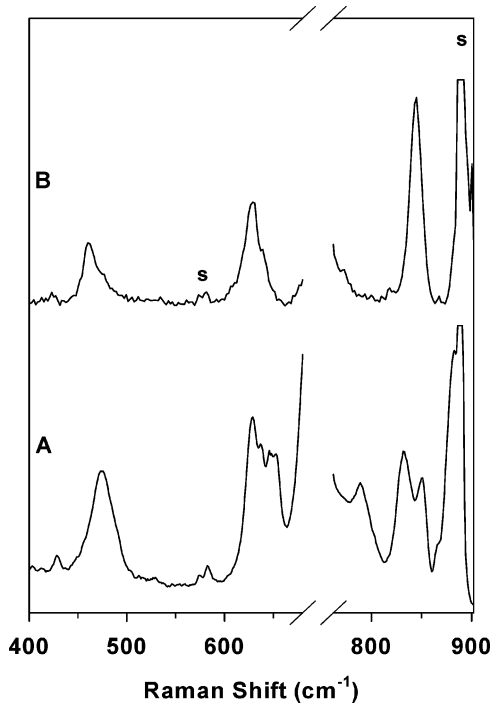

Figure 15. Raman spectra of **2** (A) and **2-OH** prepared by NEt_3 reduction of **4** (B), in frozen CH_2Cl_2 using 632.8- and 488.0-nm excitations, respectively. Peaks labeled "s" are solvent features; note the axis break to delete the more intense solvent features.

obtained for all the reduced product solutions (Figure S11 in the Supporting Information). The use of an even stronger base like K(18-crown-6)$^+$ ^{t}BuO$^-$ did not result in observable accumulation of the desired oxo(alkylperoxo)iron(IV) complex but also eventually led to generation of the orange chromophore as well.

4. Discussion

We have described herein the formation of two spectroscopically distinct high-valent intermediates by oxidation of [Fe^{II}(β-BPMCN)(OTf)$_2$] (**1**) with ^{t}BuOOH depending on solvent conditions. One is an oxoiron(IV) complex **3** in CH_3CN, precedented by several similar complexes,[17−19] and the other, a novel alkylperoxoiron(IV) complex **4** obtained in the absence of Lewis bases in cold CH_2Cl_2. The two reactions appear to be mechanistically related, where the latter product may be considered to be a simple tautomer of a ^{t}BuOOH adduct of oxoiron(IV) **3**. Analogous peroxoiron(IV) complexes have been proposed previously as key oxidizing intermediates in the reactions of various nonheme iron(II) complexes with excess H_2O_2 and ^{t}BuOOH by Sawyer and co-workers but were not directly observed.[58,59] However, **4** represents the first such peroxoiron(IV) complex to be trapped and characterized spectroscopically.

Formation of **4** from **2** might occur from either of two intermediate hydroperoxide adducts (Scheme 2). In one pathway, **2** first decomposes to yield an oxoiron(IV) complex **3-OTf** by O−O bond homolysis. Given the absence of competing Lewis bases in CH_2Cl_2, substitution of ^{t}BuOOH onto the labile sixth site of Lewis acidic **3** would occur readily, and simple tautomerization of the resulting adduct (**3-HOOR**) would yield the (alkylperoxo)(hydroxo)iron(IV) complex, **4**. Alternatively, and perhaps more plausibly, ^{t}BuOOH would bind at the iron(III) stage to form a low-spin Fe^{III}(OOR)(HOOR) adduct (**2-HOOR**) that also decays by O−O bond homolysis, yielding **3-HOOR** and then **4**. Binding of a Lewis base at the sixth coordination site of **2** should afford access to the directly observed low-spin state, thus promoting O−O bond homolysis, as shown previously for low-spin [Fe^{III}(TPA)(OO^{t}Bu)]$^{2+}$.[38] In either case, addition of excess alkyl hydroperoxide to an effectively five-coordinate complex would yield positional isomerism in which the alkylperoxide ligand is bound trans to either amine or pyridine in the unsymmetric *cis*-beta topology of BPMCN, leading to the two isomers observed for **4** (Scheme 3).[26,27] Alternative attribution of isomerism to refolding of the ligand seems unlikely given the rigid chelation of the diaminocyclohexyl backbone, which is robust even on high-spin iron(II) at room temperature. The other possibility is differential sixth site ligation, which would be subject to the significant constraints already discussed. Given differing trans donors, it is not surprising that the alkylperoxoiron(IV) isomers should exhibit distinct CT transitions, Raman modes, and NMR signals, although such isomerism has not been recognized in low-spin iron(III) complexes studied to date, including **2-NCR** herein.

The trapping of an alkylperoxoiron(IV) intermediate is nonetheless remarkable, given a plausible reduction path for iron(IV) through peroxide oxidation. Notwithstanding some difference in relative intensities, comparison of the spectroscopic properties of **4** to those of low-spin alkylperoxoiron(III) intermediates suggests comparable electronic structures, as the LMCT bands of **4** are expectedly red-shifted from those of **2-NCR** and the Raman stretching frequencies of the alkylperoxo ligands in **2** and **4** are sufficiently similar to have engendered some earlier confusion. A DFT calculation by Lehnert et al. on a simple model of low-spin alkylperoxoiron(III) complexes, *cis*-[(H$_3$N)$_4$Fe^{III}(OH$_x$)(OO^{t}Bu)]$^{x+}$ (x = 1, 2) illuminates this comparison.[37] Removal of a single electron from the metal-centered t_{2g} orbitals that comprise the β-spin HOMOs of a spin-unrestricted MO scheme would afford an S = 1 iron(IV) complex with a formulation analogous to that assigned herein to **4**. Two of these d orbitals are typically π-antibonding in oxoiron(IV) complexes, but the bent trans geometry of the alkylperoxo ligand allows donation from only one of its filled π*-orbitals. Therefore, the added t_{2g} hole will occupy an orbital that is essentially nonbonding with respect to the alkylperoxo ligand but can interact alternatively with filled p orbitals on the hydroxide, stabilizing the higher valency of the iron and damping increased σ-donation from the alkylperoxo ligand as well.

Similar considerations apply in rationalizing the recent formulation of chloroperoxidase Compound II as an iron(IV) complex with axial hydroxide and thiolate ligands.[60] The pertinent issue is the oxo basicity required to stabilize the analogous hydroxo/alkylperoxo tautomeric structure in **4**. Such basicity may be fundamentally important, for example, in dioxygen reduction by synthetic nonheme complexes as well.[61] The anionic heme and thiolate ancillary ligation of chloroper-

(56) Sohn, Y. S.; Hendrickson, D. N.; Gray, H. B. *J. Am. Chem. Soc.* **1971**, *93*, 3603−3612.
(57) Connelly, N. G.; Geiger, W. E. *Chem. Rev.* **1996**, *96*, 877−910.
(58) Tung, H.-C.; Kang, C.; Sawyer, D. T. *J. Am. Chem. Soc.* **1992**, *114*, 3445−3455.
(59) Sawyer, D. T.; Sobkowiak, A.; Matsushita, T. *Acc. Chem. Res.* **1996**, *29*, 409−416.
(60) Green, M. T.; Dawson, J. H.; Gray, H. B. *Science* **2004**, *304*, 1653−1656.
(61) MacBeth, C. E.; Golombek, A. P.; Young, V. G., Jr.; Yang, C.; Kuczera, K.; Hendrich, M. P.; Borovik, A. S. *Science* **2000**, *289*, 938−941.

Scheme 2. Proposed Pathways for Conversion of **2** to **4** (Only One Positional Isomer Shown)

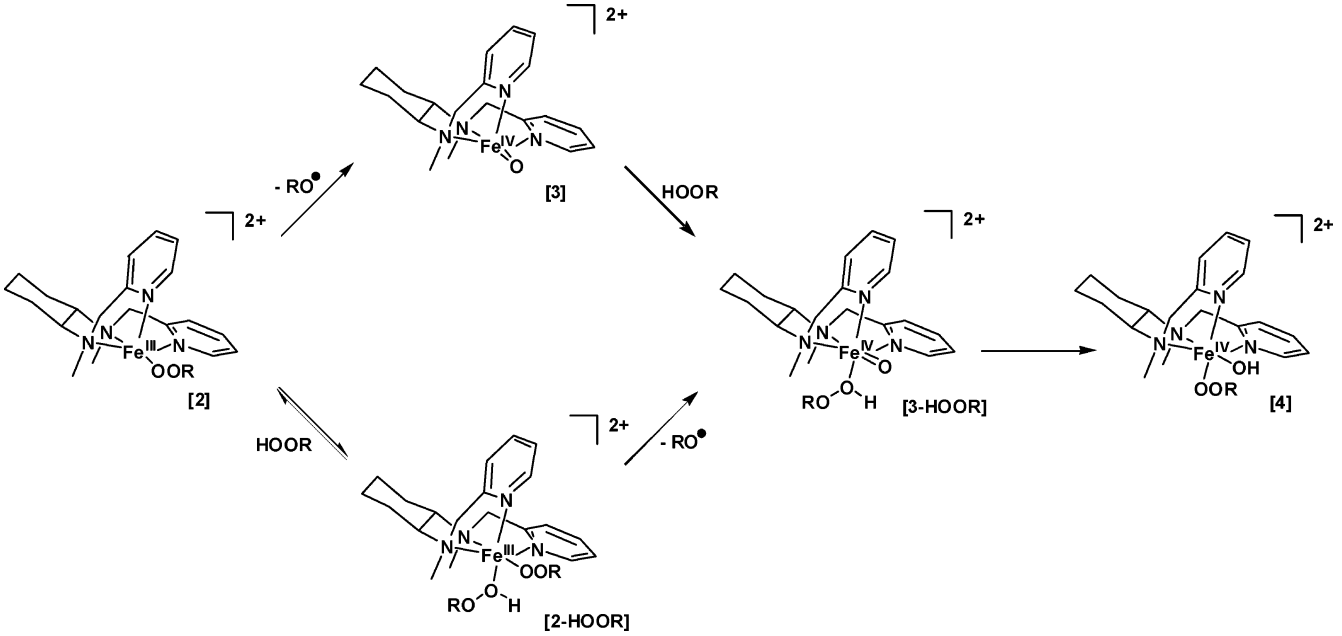

Scheme 3. Proposed Positional Isomerism of **4**

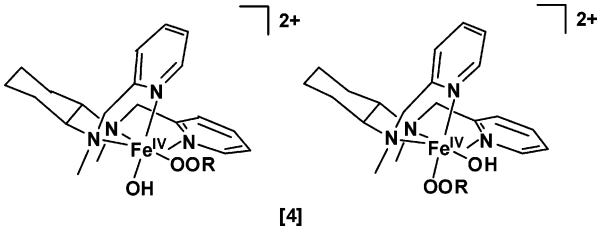

oxidase impart significant basicity to the oxoiron(IV) center in the so-called compound II intermediate, providing additional thermodynamic driving force for the archetypical H-atom abstraction from strongly covalent hydrocarbon substrates to the formally oxoiron(V) center of the reactive compound I intermediate.[1] The neutral supporting ligation in the present work affords dicationic oxoiron(IV) intermediates, but ^{t}BuOOH is considerably more acidic than hydrocarbons, particularly when activated by direct ligation to the Lewis acidic iron center, and this effect seems adequate to stabilize a cis hydroxo/peroxo tautomer **4** relative to **3-HOOR** in cold CH_2Cl_2 solution.

In summary, the reaction of **1** with ^{t}BuOOH in CH_3CN and CH_2Cl_2 affords two distinct iron(IV) species **3** and **4**, respectively. While the oxoiron(IV) unit in **3** is now well precedented in other complexes of tetradentate and pentadentate ligands,[17−19] **4** represents a unique nonheme ligand environment for the iron(IV) oxidation state, adding to the number of recognized nonheme iron(IV)−oxygen motifs, which now include (oxo)iron(IV),[17−19] (μ-oxo)diiron(IV),[21] and (hydroxo)(peroxo)iron(IV). Furthermore, **4** might serve as a useful precursor for trapping of the nonheme oxoiron(V) species that have been invoked in a number of bio-inspired nonheme iron stereospecific oxidation reactions, for which there is now only indirect mechanistic evidence.[62,63]

Acknowledgment. This work was supported by the National Institutes of Health (GM-33162 and GM-38767 to L.Q. and EB-001475 to E.M.). M.C. and J.-U.R. thank Fundacio La Caixa and the Deutsche Forschungsgemeinschaft (DFG), respectively, for postdoctoral fellowships. A.S. is a recipient of a Graduate Research Fellowship from the National Science Foundation. XAS data were collected on beamline X9B at the National Synchrotron Light source or on beamline 7-3 of the Stanford Synchrotron Radiation Laboratory, both supported by the Department of Energy and the NIH Research Resource Program. Stock solutions of ^{t}Bu^{16}O^{18}OH and ^{t}Bu^{18}O^{18}OH were the generous gifts of Dr. Evan Appelman (Argonne National Laboratory) and Prof. Kiyoshi Fujisawa (Tsukuba University, Japan), respectively. We thank Dr. Letitia Yao and Michael R. Bukowski, respectively, for technical assistance with ^{2}H NMR and ESI-MS experiments. We also thank Dr. Matthew J. Latimer (SSRL) and Dr. Nebojsa S. Marinkovic (NSLS) for technical support of synchrotron experiments.

Supporting Information Available: Raman spectra of isotopic **2** in CH_3CN and CH_2Cl_2, additional details of the EXAFS and Mössbauer analyses, full electrospray ionization mass spectra of **4** in CH_2Cl_2 and PrCN, Raman spectra of reduced **4** in CH_2Cl_2. This material is available free of charge via the Internet at http://pubs.acs.org.

JA0438765

(62) Chen, K.; Que, L., Jr. *J. Am. Chem. Soc.* **2001**, *123*, 6327−6337.
(63) Chen, K.; Costas, M.; Kim, J.; Tipton, A. K.; Que, L., Jr. *J. Am. Chem. Soc.* **2002**, *124*, 3026−3035.